Nuclear–cytoskeletal linkages facilitate cross talk between the nucleus and intercellular adhesions

Rachel M. Stewart,[1] Amanda E. Zubek,[2,3] Kathryn A. Rosowski,[3] Sarah M. Schreiner,[1] Valerie Horsley,[2,3] and Megan C. King,[1]

[1]Department of Cell Biology and [2]Department of Dermatology, Yale School of Medicine; and [3]Department of Molecular, Cell and Developmental Biology; Yale University, New Haven, CT, 06520

The linker of nucleoskeleton and cytoskeleton (LINC) complex allows cells to actively control nuclear position by coupling the nucleus to the cytoplasmic cytoskeleton. Nuclear position responds to the formation of intercellular adhesions through coordination with the cytoskeleton, but it is not known whether this response impacts adhesion function. In this paper, we demonstrate that the LINC complex component SUN2 contributes to the mechanical integrity of intercellular adhesions between mammalian epidermal keratinocytes. Mice deficient for *Sun2* exhibited irregular hair follicle intercellular adhesions, defective follicle structure, and alopecia. Primary mouse keratinocytes lacking *Sun2* displayed aberrant nuclear position in response to adhesion formation, altered desmosome distribution, and mechanically defective adhesions. This dysfunction appeared rooted in a failure of *Sun2*-null cells to reorganize their microtubule network to support coordinated intercellular adhesion. Together, these results suggest that cross talk between the nucleus, cytoskeleton, and intercellular adhesions is important for epidermal tissue integrity.

Introduction

Keratinocytes comprise most of the mammalian epidermis and its appendages, such as the hair follicle, and must withstand substantial mechanical stress to effectively function as the body's protective barrier against pathogen invasion and dehydration (Madison, 2003). The mechanical integrity of the epidermis requires tight cell–cell and cell–ECM adhesions. Indeed, the loss or disruption of cadherin-based intercellular adhesions, such as adherens junctions (AJs) or desmosomes, or integrin-based cell–ECM junctions, such as focal adhesions and hemidesmosomes, results in defects in skin barrier function and hair follicle structure (Simpson et al., 2011).

Both cell–cell and cell–ECM adhesions are mechanosensitive (Galbraith et al., 2002; le Duc et al., 2010; Yonemura et al., 2010) and are capable of transducing externally applied force (Grashoff et al., 2010; Borghi et al., 2012; Mertz et al., 2013) and responding to mechanical stimulation (Pelham and Wang, 1997; Riveline et al., 2001; Oakes et al., 2012). Tension at cadherin-based junctions can elicit cell-signaling events (Vaezi et al., 2002; le Duc et al., 2010; Yonemura et al., 2010), alter actin dynamics (le Duc et al., 2010; Yonemura et al., 2010; Niessen et al., 2011; Hong et al., 2013; Engl et al., 2014), and coordinate mechanical behavior across multiple cells (Trepat et al., 2009; Maruthamuthu et al., 2011; Mertz et al., 2012, 2013). Although proteins that link intercellular junctions to cytoskeletal elements respond to mechanical stimuli at the cell membrane (le Duc et al., 2010; Yonemura et al., 2010; Ray et al., 2013), the mechanisms that allow forces to be coordinated within the cell to support epidermal homeostasis are largely unknown.

Interestingly, cadherin-based cell–cell adhesions in epithelial cells can alter nuclear position (Dupin et al., 2009), suggesting a link between intercellular junctions and the nucleus. An interconnected cytoskeletal network linking cell–cell adhesions to cell–ECM adhesions may be integrated at the nucleus through nuclear envelope (NE)–spanning linker of nucleoskeleton and cytoskeleton (LINC) complexes (Wang et al., 2009; Simon and Wilson, 2011). The well-conserved LINC complex consists of SUN (Sad1/UNC-84) domain proteins embedded in

Correspondence to Megan C. King: megan.king@yale.edu; or Valerie Horsley: valerie.horsley@yale.edu

Abbreviations used in this paper: AJ, adherens junction; ANOVA, analysis of variance; CCD, charge-coupled device; DPI/II, desmoplakin I/II; Dsg4, desmoglein 4; E-cad, E-cadherin; He, Henle; Hu, Huxley; IRS, inner root sheath; K14, keratin 14; LINC, linker of nucleoskeleton and cytoskeleton; MKC, mouse keratinocyte; MT, microtubule; NE, nuclear envelope; ORS, outer root sheath; TEM, transmission EM; WT, wild type.

The Rockefeller University Press $30.00
J. Cell Biol. Vol. 209 No. 3 403–418
www.jcb.org/cgi/doi/10.1083/jcb.201502024

the inner nuclear membrane, coupled to KASH (Klarsicht/ANC-1/Syne homology) domain proteins, the Nesprins or SYNEs in mammals, located in the outer nuclear membrane (Sosa et al., 2012). Although SUN1 and SUN2 interact with lamins, other inner nuclear membrane proteins, and chromatin inside the nucleus, Nesprin-1, -2, and -3 associate with actin, microtubules (MTs), and/or intermediate filaments in the cytoplasm (Sosa et al., 2012). LINC complexes, by transducing force from the cytoskeleton to the nuclear interior, mediate nuclear migration and anchorage in various mammalian tissues (Zhang et al., 2007; Lei et al., 2009; Yu et al., 2011; Razafsky et al., 2012) and have the potential to act as conduits for nuclear mechanotransduction (Dahl et al., 2008; Wang et al., 2009; Brosig et al., 2010; Guilluy et al., 2014). Mice expressing a mutant form of Nesprin-2 Giant lacking its actin binding domains displayed defective nuclear morphology in epidermal keratinocytes and delayed wound healing in vivo (Lüke et al., 2008; Rashmi et al., 2012). These data hint at the necessity of functional nuclear–cytoskeletal linkages in supporting the epidermis, although extensive examination of LINC complex function in the epidermis has not been performed to date.

Here, we define a role for LINC complexes in supporting epidermal keratinocyte cytoskeletal organization and intercellular adhesion and, thereby, the mechanical integrity of the murine hair follicle. *Sun2*-null mice displayed defects in follicle structure, which lead to transient alopecia. Primary keratinocytes derived from *Sun2*-null mice failed to reorganize the MT cytoskeleton or properly control nuclear position in response to adhesion formation, exhibited defective desmosome distribution at cell–cell junctions, and had impaired mechanical stability of intercellular adhesions. Ultrastructural analysis revealed that alterations in desmosome number and structure also occurred between *Sun2*-null follicular trichocytes in vivo. These results implicate LINC complexes, and therefore nuclear–cytoskeletal interactions, in supporting the strength of cell–cell adhesions and the overall mechanical integrity of the epidermis.

Results

SUN2 is expressed in the epidermis and hair follicle

To characterize the expression of SUN domain-containing proteins of the LINC complex in the skin, we immunostained back skin from wild-type (WT) mice for the broadly expressed SUN1 and SUN2 proteins. SUN1 was primarily found in the basal and suprabasal layers of the epidermis at the NE but was absent from the hair follicle at postnatal day 4 (P4; Fig. 1 A, arrows). Prominent expression of SUN2, also localized to the NE, was detected throughout the epidermis and dermis, as well as through all layers of the hair follicle, at P4 (Fig. 1 B and Fig. S1, A and B). SUN2 continued to be robustly expressed in the regressing hair shaft at P17 and the regrown hair follicle at P32 (Fig. S1, C and D).

Sun2$^{-/-}$ mice exhibit alopecia and abnormal hair follicle morphology

Given the postnatal lethality of *Sun1/Sun2* double-null mice (Lei et al., 2009) and our finding that SUN2 was the primary SUN domain-containing protein expressed in the hair follicle (Fig. 1, A and B), we used a *Sun2*-null mouse model (which lacked exons 11–16, including the SUN domain) to investigate the consequences of disrupting LINC complex function in the epidermis (Lei et al., 2009). As in the original publication, we refer to this mouse as *Sun2*$^{-/-}$. We note that a truncated fragment of SUN2 lacking the SUN domain could be expressed in these mice but would be incapable of interacting with Nesprins (Lei et al., 2009). As originally described, *Sun2*$^{-/-}$ mice did not display any overt phenotypic abnormalities at birth, and skin sections from *Sun2*$^{-/-}$ mice revealed an absence of SUN2 staining, as assessed with an antibody raised to the C-terminal SUN domain (Fig. S1, E and F). Strikingly, these mice displayed progressive hair loss beginning at P16 (Fig. 1 C). In contrast, *Sun1*$^{-/-}$ mice (Ding et al., 2007) did not exhibit alopecia (Fig. S1 G).

To elucidate the origin of the alopecia phenotype in *Sun2*$^{-/-}$ mice, we examined the morphology of WT and *Sun2*$^{-/-}$ hair follicles in histological sections during the first hair cycle (Fig. 1 D). Although *Sun2*$^{-/-}$ follicles displayed grossly normal morphology at P4 (Fig. 1 D, I and II), hair shaft breakages were observed at P16 (Fig. 1 D, III–VI, arrow) and P18 (Fig. 1, D [VII–X, arrow] and E). In contrast, histological analysis of follicles from *Sun1*$^{-/-}$ mice revealed no structural differences compared with WT follicles (Fig. S1 G).

To determine whether structural changes to the hair follicle occurred during follicular morphogenesis in *Sun2*$^{-/-}$ mice, we analyzed skin sections from WT and *Sun2*$^{-/-}$ mice at P4, when all of the follicles have entered into a mature growth stage. We found that trichocytes in *Sun2*$^{-/-}$ follicles formed the differentiated layers of the hair follicle normally (Fig. S1, H and I). However, closer analysis of the keratin 6–positive companion layer demonstrated that *Sun2*$^{-/-}$ follicles were extensively bent compared with the aligned structure of WT follicles (Fig. 1, F, G [arrows], and H). These bends extended to the outer root sheath (ORS) in *Sun2*$^{-/-}$ follicles (Fig. S1, H and I, arrowhead). By P32, *Sun2*$^{-/-}$ mice regained a normal hair coat that was maintained over the course of their remaining life span, and follicles at this age exhibited no gross morphological defects (Fig. 1, C and D, XI and XII). Together, these results indicate that SUN2 is required for the maintenance of normal hair follicle structure during the first hair cycle.

Nuclear position is influenced by intercellular adhesion and SUN2

Given the established role for the LINC complex in regulating nuclear position, we examined this process in the context of a cultured epidermal keratinocyte model. In this system, the formation of cadherin-based adhesions in primary mouse keratinocytes (MKCs) is driven by the elevation of extracellular calcium (Ca^{2+}). We first established that both SUN1 and SUN2 were expressed in isolated WT MKCs, although the relative expression levels of the two SUN proteins could not be determined (Fig. S2 A). MKCs derived from the *Sun2*$^{-/-}$ mouse model lacked SUN2 expression, whereas SUN1 was expressed at comparable levels in both WT and *Sun2*$^{-/-}$ MKCs (Fig. S2 A).

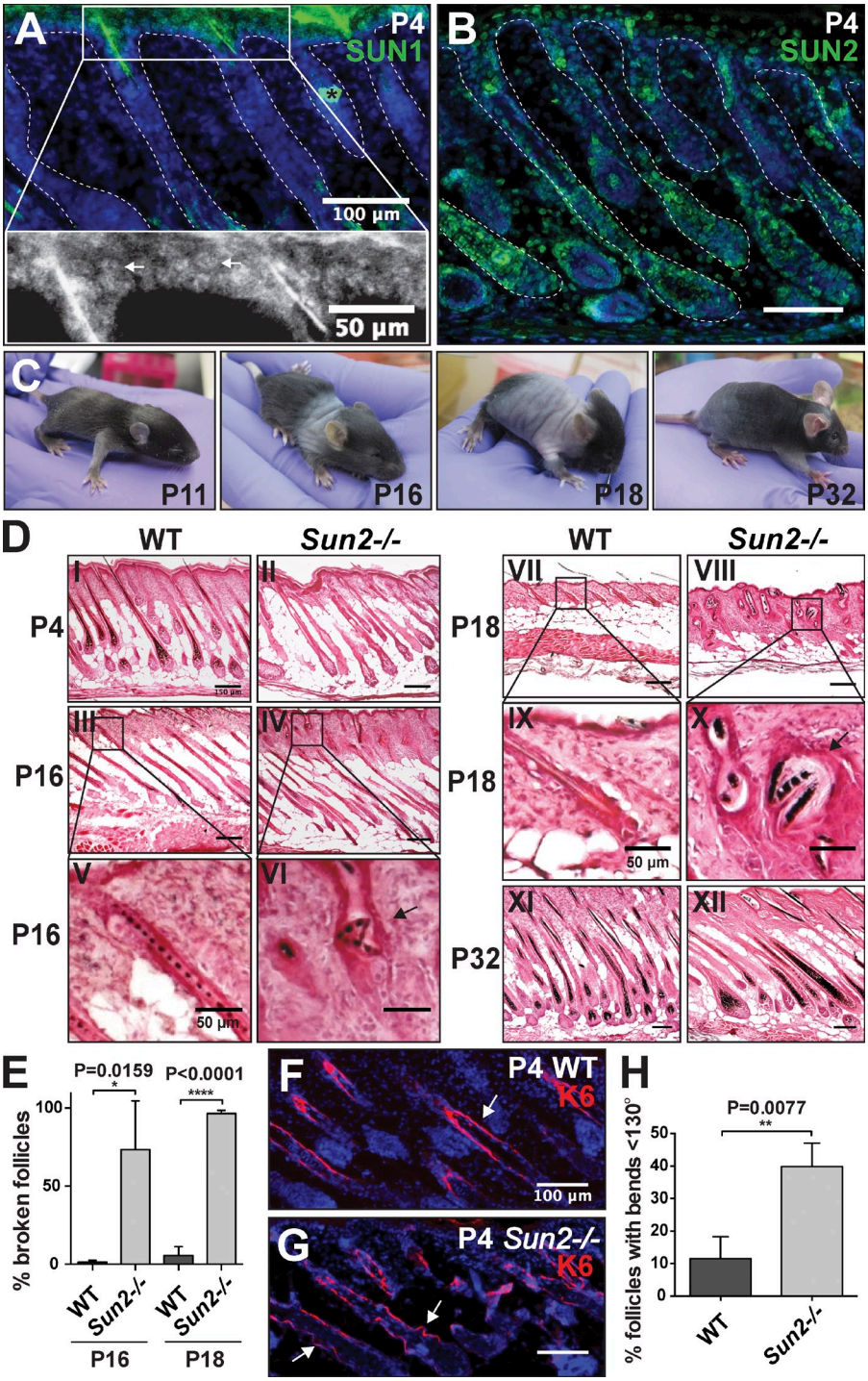

Figure 1. ***Sun2*$^{-/-}$ mice exhibit alopecia and abnormal hair follicle structure.** (A) Immunostaining of mouse back skin revealed NE localized SUN1 (also greyscale inset, arrows) was expressed in the epidermis. Asterisk indicates nonspecific staining. Dotted lines delineate hair follicles. (B) SUN2 was strongly expressed in the epidermis, dermis, and hair follicle. Dotted lines delineate hair follicles. Bar, 100 µm. (C) *Sun2*$^{-/-}$ mice developed alopecia at P16 yet regained a normal coat by the second hair cycle (P32). (D) Hematoxylin and eosin–stained back skin from WT and *Sun2*$^{-/-}$ mice show hair shaft breaks at P16 (IV and VI, arrow) and P18 (VIII and X, arrow). (E) Quantification of broken follicles in WT and *Sun2*$^{-/-}$ mice. $n > 160$ follicles in three mice per genotype. (F and G) Immunostaining of back skin from WT and *Sun2*$^{-/-}$ mice for keratin 6 (K6) and Hoechst illustrated acute bends in *Sun2*$^{-/-}$ follicles (G, arrows), whereas WT follicles remained linear (F, arrow). (H) Percentage of total follicles with at least one bend <130°. $n > 98$ follicles in three mice per genotype. Error bars indicate SDs. Statistical significance determined by unpaired, two-tailed *t* test.

Furthermore, SUN2 localized to the NE before and after calcium-induced adhesion formation (Fig. 2 A).

To determine how nuclear position would respond to the formation of intercellular adhesions, we measured the distance between the centroids of the cell and nucleus in MKCs at the periphery of small colonies that featured a "free" edge (Fig. 2 B, black cells). Before Ca^{2+} addition, WT MKCs maintained the nucleus at the cell center (Fig. 2, C and E). However, 12–24 h after the induction of intercellular adhesion, the nucleus progressively moved away from the cell center toward "interior" cell–cell adhesions (Fig. 2, B [magenta adhesions], D, and E), an effect previously seen in epithelial cell lines (Dupin et al., 2009). Here, we define interior adhesions as those located close to the colony center and "lateral" adhesions (Wu et al., 2014) as those adjacent to the colony free edge (Fig. 2 B; see also Fig. 5 E). The nuclear positioning bias toward interior cell–cell adhesions was only observed in cells with free edges (Fig. 2 B, black cells), whereas cells with contacts on all sides displayed centrally located nuclei (Fig. 2, D [arrow] and E). A reorganization of cytoskeleton-dependent tension across MKC colonies occurs on a similar timescale (Mertz et al., 2013), suggesting that the changes in

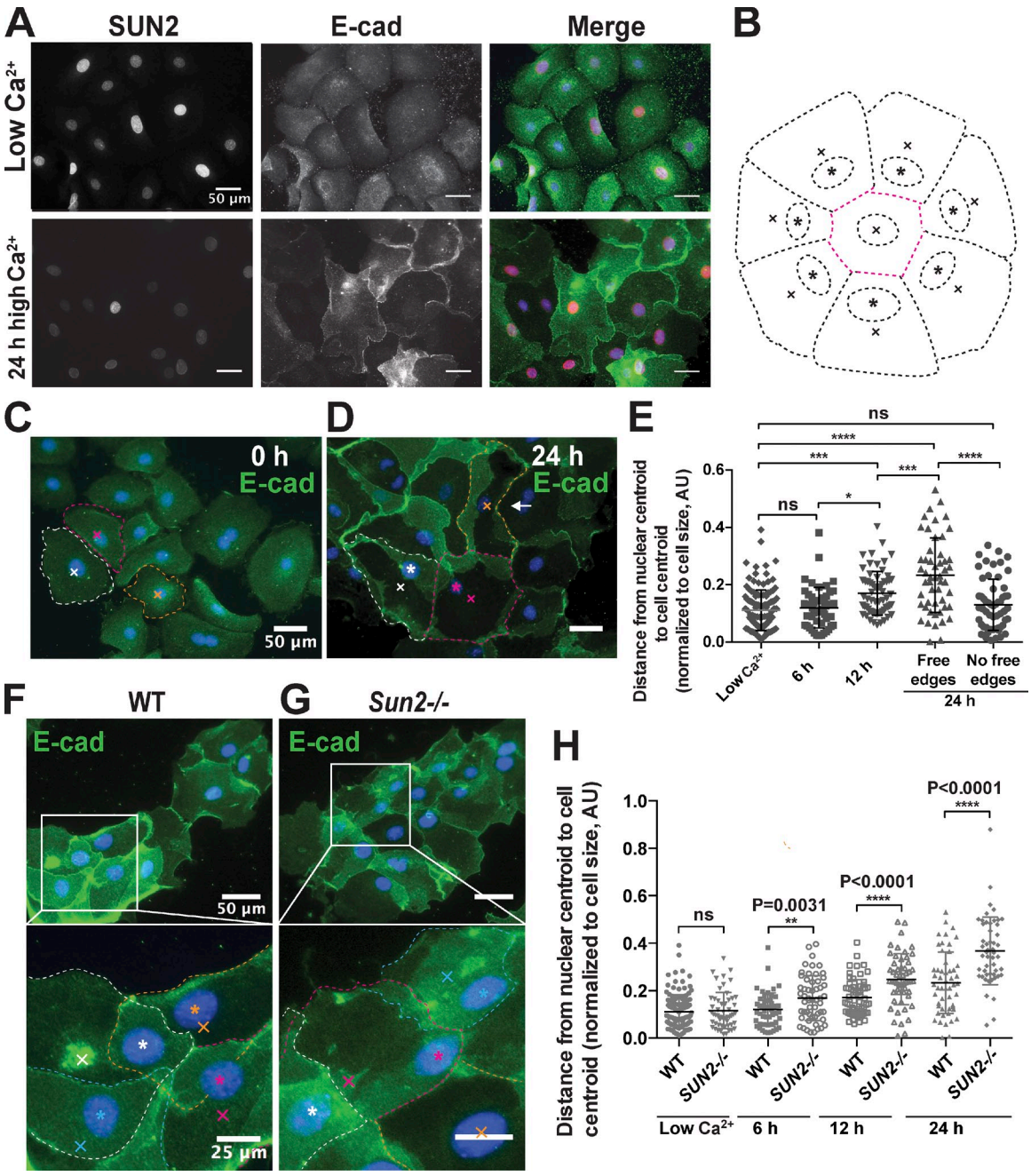

Figure 2. **Adhesion-dependent nuclear movement occurs in WT epidermal MKCs and is exaggerated in *Sun2*$^{-/-}$ MKCs.** (A) SUN2 and E-cadherin (E-cad) localization in WT MKCs in low calcium (Ca^{2+}) or in high Ca^{2+} medium for 24 h. (B) Diagram of a MKC colony illustrating interior adhesions (magenta) at cell–cell contacts opposite from the free edge in cells at the colony periphery. Nuclear position (asterisks) is biased toward interior adhesions and away from the cell centroid (marked with x's). (C and D) E-cad and nuclear position in WT MKCs cultured in high Ca^{2+} medium for 0 and 24 h. Each cell periphery is outlined (dotted lines), and the nuclear centroid (asterisks) and cell centroid (x's) are shown in matching colors. Arrow in D indicates a cell without a free edge with a central nuclear position. (E) Plots of the nuclear centroid to cell centroid distance normalized to cell radius during MKC adhesion formation at indicated time points after Ca^{2+} addition. $n > 50$ cells per time point (representative of three experiments). Error bars indicate SDs. Asterisks denote indicated significance (*, $P \leq 0.05$; ***, $P \leq 0.001$; ****, $P \leq 0.0001$; ANOVA with Tukey's posttest). (F and G) E-cad and nuclear position in WT and *Sun2*$^{-/-}$ MKCs cultured in high Ca^{2+} medium for 24 h. Nuclei (asterisks) directly abut E-cad–positive AJs (dotted lines) in *Sun2*$^{-/-}$ MKCs at colony edges (G, inset). (H) Quantification of nuclear position as in E for WT and *Sun2*$^{-/-}$ MKCs. $n > 50$ cells per genotype at each time point (representative of three experiments). Error bars indicate SDs. Statistical significance determined by unpaired, two-tailed *t* test. AU, arbitrary unit.

nuclear position may reflect cytoskeletal forces that coordinate cell–cell and cell–ECM adhesions.

Next, we assessed whether the adhesion-dependent nuclear movement is influenced by loss of SUN2. Both WT and *Sun2*$^{-/-}$ MKCs exhibited E-cadherin (E-cad) recruitment to regions of cell–cell contact after Ca^{2+} addition (Fig. 2, F and G). We analyzed the nuclear position of WT and *Sun2*$^{-/-}$ MKCs at the edges of colonies after 0, 6, 12, and 24 h in high Ca^{2+}

medium (Fig. 2, F–H; and Fig. S2 B). As expected, nuclei were centrally located in both WT and *Sun2*$^{-/-}$ MKCs before adhesion formation (Figs. 2 H and S2 B). In contrast to WT MKCs, the nuclei of *Sun2*$^{-/-}$ MKCs exhibited a closer association with interior intercellular junctions at all time points after Ca^{2+} addition and directly abutted these junctions at 24 h (Fig. 2, G and H). Thus, loss of *Sun2* influences adhesion-dependent nuclear position in MKCs, possibly by impacting the association of the cytoskeleton with the NE.

Actomyosin contractility drives adhesion-induced nuclear movement, whereas MTs counteract this movement

To examine whether the cytoskeleton influences the nuclear response to adhesion formation, we treated WT MKCs with a variety of pharmacologic agents during the induction of intercellular adhesion by Ca^{2+} addition (Fig. 3 A). Treating WT MKCs during adhesion formation with inhibitors of actomyosin contractility, including the myosin II inhibitor blebbistatin (Fig. 3, B and C) and the Rho-associated protein kinase inhibitor Y-27632 (Fig. S2, C and D), prevented the typical movement of nuclei toward interior junctions (Fig. 3 C and Fig. S2 D). The mean cell centroid to nuclear centroid distance observed in these treated cells mimicked that seen in cells before adhesion formation (~0.1), indicating that the nuclei were centrally located. In contrast, depolymerization of MTs with nocodazole before adhesion formation resulted in an unusually strong bias in nuclear position toward interior junctions (Fig. 3, B and D). Interestingly, nuclear position in cells treated with both blebbistatin (or Y-27632; Fig. S2, C and D) and nocodazole did not differ from control cells (Fig. 3, B and D). These observations suggest that actomyosin contractility promotes the movement of nuclei toward interior adhesions, whereas the MT cytoskeleton attenuates this movement.

Because disruption of the cytoskeleton can compromise AJ, desmosome, and focal adhesion formation and dynamics (Gardel et al., 2010; Harris and Tepass, 2010; Nekrasova and Green, 2013), we next examined the impact of cytoskeletal disruption on nuclear position after mature adhesions had formed (Fig. 3 E). Treatment of MKCs with blebbistatin or Y-27632 after adhesion formation had little effect on nuclear position, which remained biased toward interior junctions (Fig. 3, F and G; and Fig. S2, E and F). However, depolymerization of the actin cytoskeleton with latrunculin A reduced the positioning bias, and nuclei moved to a more central position (Fig. 3, F and G). Again, MT depolymerization with nocodazole led to unusually close apposition of nuclei and interior junctions after adhesion formation (Fig. 3, F and H). Concomitant depolymerization of MTs and inhibition of actomyosin contractility after adhesion formation led to a more central nuclear position (Fig. 3, F and H; and Fig. S2, E and F), although this effect did not fully recapitulate the results seen with drug addition before Ca^{2+} addition (Fig. 3 D). Thus, an intact actin network is required to maintain nuclei at interior junctions after adhesion formation, whereas myosin activity is not. Furthermore, MTs appear to have a dynamic function in promoting a more centrally positioned nucleus by opposing actomyosin-based forces.

Sun2$^{-/-}$ MKCs fail to reorganize the MT cytoskeleton upon adhesion formation

Interestingly, nuclear position in nocodazole-treated WT MKCs mimicked the nuclear positioning defect in *Sun2*$^{-/-}$ MKCs, suggesting that alterations in the MT cytoskeleton may contribute to this phenotype. To test this, we first analyzed cytoskeletal organization in WT MKCs (Fig. 4 A). The steady-state distribution of MTs was similar before and after formation of intercellular adhesions, although a denser enrichment of perinuclear MTs was observed in cells after 24 h of Ca^{2+} exposure (Fig. 4 A, β-tubulin images, arrows). In addition, we found that MTs accumulated along the cell periphery 24 h after Ca^{2+} addition, appearing similar to the lamella-localized MTs observed in migratory cells (Wittmann and Waterman-Storer, 2005), whereas most MTs were found orthogonal to the cell cortex in low Ca^{2+} (Fig. 4, A, B [arrowheads], and C). These observations are consistent with the adhesion-dependent reorganization of MT-regulatory proteins that has previously been described (Lechler and Fuchs, 2007; Sumigray et al., 2011, 2012). The F-actin cytoskeleton, as assessed by phalloidin staining, and actomyosin contractility, as assessed by phosphorylated myosin light chain staining, were predominantly organized as stress fibers along the cell periphery under both Ca^{2+} conditions (Fig. 4 A). We also observed the formation of a keratin 14 (K14) perinuclear cage 24 h after Ca^{2+} addition (Fig. 4 A, arrows), as expected (Lee et al., 2012).

We next asked whether *Sun2*$^{-/-}$ MKCs recapitulated the cytoskeletal rearrangements observed in WT cells upon adhesion formation. Cytoskeletal organization before Ca^{2+} addition did not differ greatly between WT and *Sun2*$^{-/-}$ MKCs, except for a modest increase in stress fibers in *Sun2*$^{-/-}$ cells (Fig. S2 G). However, we observed two defects in the steady-state distribution of MTs in *Sun2*$^{-/-}$ MKCs after Ca^{2+} addition (Fig. 4, B–D): first, the perinuclear cage of MTs was often substantially less intense (Fig. 4, A and D, β-tubulin images, arrows) and second, the enrichment of adhesion-induced MTs along the cell periphery was reduced (Fig. 4, A–D, arrowheads). We also observed a modest increase in the number of stress fibers passing through the cell center, along with normal stress fiber staining at the cortex (Fig. 4 D). A perinuclear K14 cage and K14 localization at junctions were also seen, along with an increase in a nuclear keratin pool (Fig. 4 D).

We reasoned that MT dynamics, in addition to steady-state MT organization, may be altered in *Sun2*$^{-/-}$ MKCs, especially in the context of the MT reorganization that occurs upon adhesion formation (Lechler and Fuchs, 2007; Sumigray et al., 2011, 2012). Taxol-treated WT MKCs exhibited stabilized MTs at intercellular junctions and cell-free edges, as previously described (Fig. 4 E, β-tubulin images [arrows] and I [arrow]; Sumigray et al., 2012). In addition, we observed a pool of stabilized MTs at the NE (Fig. 4 E, III, arrow). In contrast, taxol-treated *Sun2*$^{-/-}$ MKCs exhibited severe disruption of both adhesion-associated and NE-associated MT pools (Fig. 4 E, β-tubulin images [arrows], I and II [arrows], and III and IV [arrows]). This result suggests that modulation of MTs at the NE and cell cortex may be mechanistically linked, and both are affected by loss of *Sun2*.

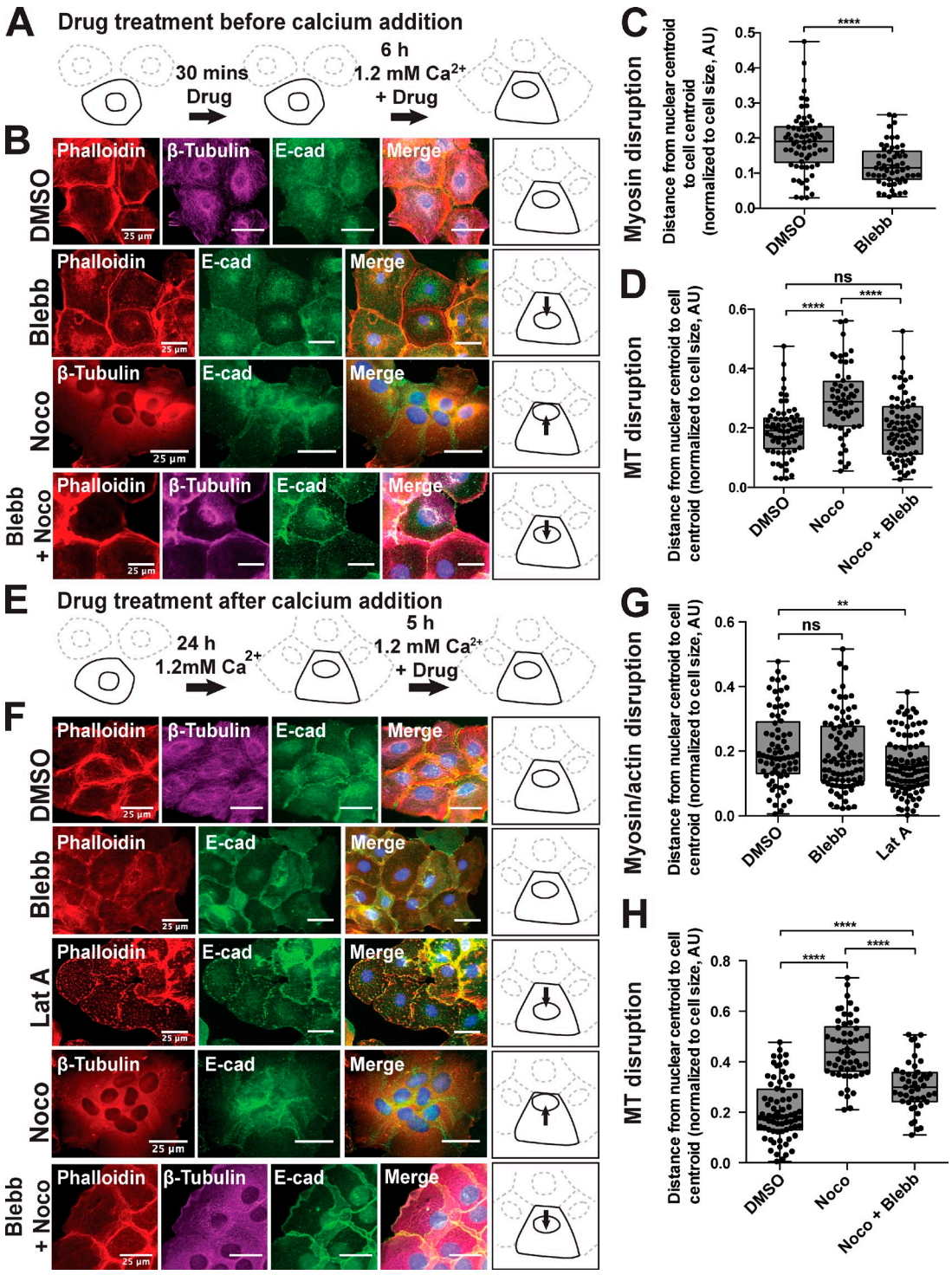

Figure 3. **Adhesion-dependent nuclear movement is differentially regulated by the actin and MT cytoskeletons.** (A) Diagram illustrating treatment of WT MKCs with the indicated drug before Ca^{2+} addition in B–D. (B) E-cadherin (E-cad; green), β-tubulin (magenta), actin (phalloidin, red), and nuclei (Hoechst) localization are shown. Diagrams illustrate the effect of drug treatment on nuclear position. (C and D) Plots of the nuclear centroid to cell centroid distance normalized to cell radius. $n > 50$ cells per condition (representative of three experiments). Nuclei in blebbistatin-treated cells remained located at the cell center. Nuclei in nocodazole-treated cells moved closer to adhesions than in DMSO-treated cells, which was rescued by blebbistatin treatment. (E) Diagram illustrating treatment of WT MKCs with the indicated drug after Ca^{2+} addition in F–H. (F) Staining as in B. (G and H) Quantification as in C and D. $n > 50$ cells per condition (representative of three experiments). Nuclear position was unaltered in blebbistatin-treated cells, whereas latrunculin A reduced nuclear movement. Nuclei in nocodazole-treated cells moved closer to adhesions than in control cells, which were partially rescued by blebbistatin. Asterisks denote indicated significance (**, $P \leq 0.01$; ****, $P \leq 0.0001$) as assessed by unpaired, two-tailed *t* test (C), ANOVA with Tukey's posttest (D and H), or ANOVA with Dunnett's posttest (G). All data plotted as box and whiskers plots; the bottom and top of the box display the 25th and 75th percentiles, whereas the central band represents the median. The whiskers indicate the minimum and maximum values, and the plus signs indicate the means. AU, arbitrary unit; Noco, nocodazole; Blebb, blebbistatin; Lat A, Latrunculin A.

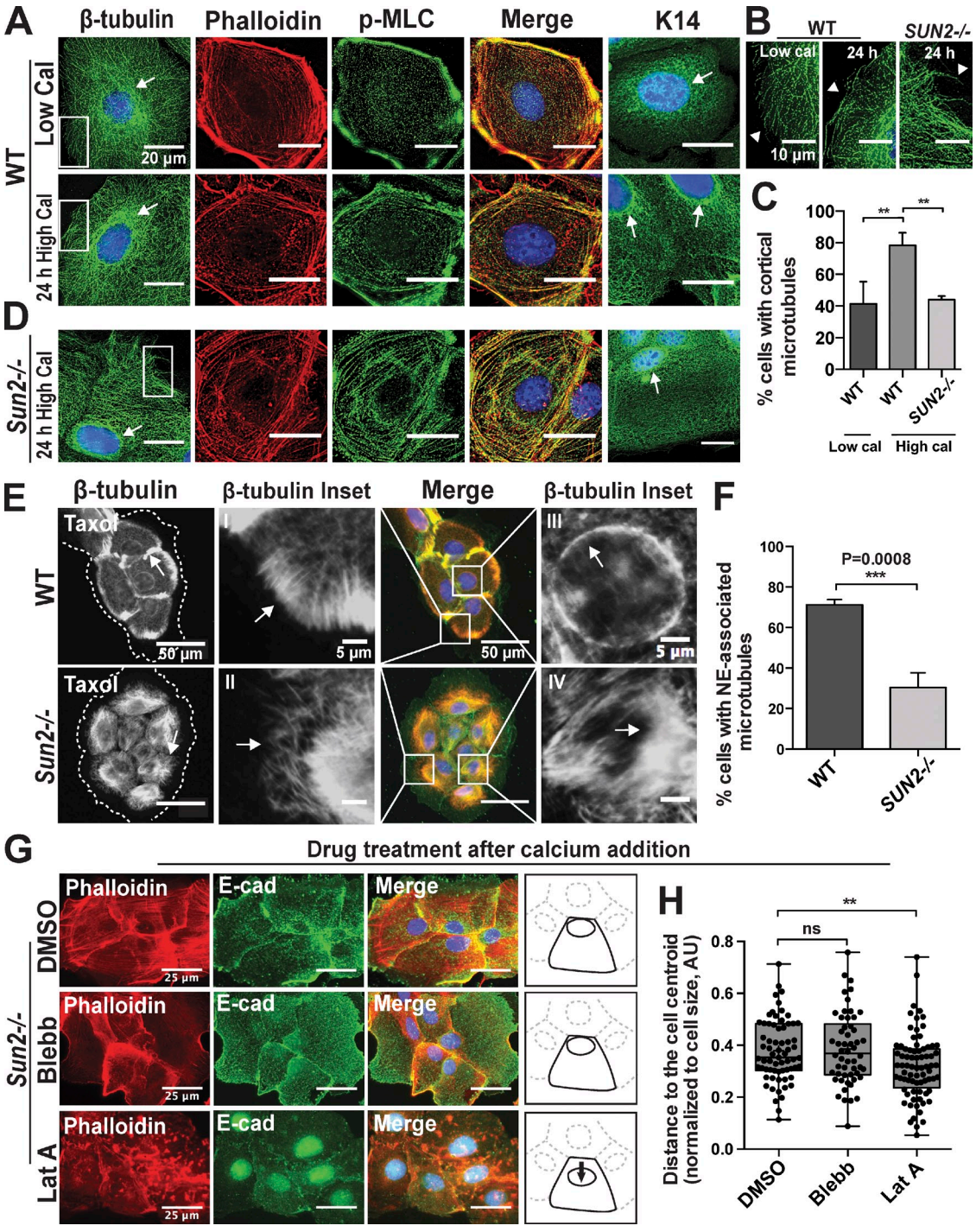

Figure 4. **Organization of the MT cytoskeleton is perturbed in differentiated *Sun2*$^{-/-}$ keratinocytes.** (A) Localization of β-tubulin, phosphorylated myosin light chain (p-MLC), keratin 14 (K14), actin (phalloidin), and nuclei (Hoechst) in WT MKCs. (B) Insets of β-tubulin localization in white boxes in A and D. Arrowheads indicate MT organization at the cell periphery. (C) Quantification of the percentage of WT or *Sun2*$^{-/-}$ MKCs in the indicated media with cortical accumulation of MTs. $n > 200$ cells per condition or genotype from three experiments. Asterisks denote indicated significance (**, $P < 0.01$; ANOVA with Dunnett's posttest). Error bars indicate SDs. (D) Staining as in A for *Sun2*$^{-/-}$ MKCs in high Ca^{2+} medium after 24 h. Arrows in β-tubulin images indicate a perinuclear β-tubulin cage in WT cells that is often lacking in *Sun2*$^{-/-}$ MKCs. Arrows in K14 images indicate a perinuclear K14 cage in both WT and *Sun2*$^{-/-}$ MKCs. (E) Localization of β-tubulin, E-cad, and nuclei (Hoechst) after 5 h of taxol treatment in WT or *Sun2*$^{-/-}$ MKCs. Arrows indicate intercellular junctions (β-tubulin images), cell periphery (I and II), or NE (III and IV). Note the lack of MT accumulation at these sites in *Sun2*$^{-/-}$ MKCs. Dashed lines indicate the colony periphery defined by E-cad staining. (F) Quantification of the percentage of WT and *Sun2*$^{-/-}$ MKCs with a stabilized pool of NE-associated MTs. $n > 200$ cells from three experiments. Error bars indicate SDs. Statistical significance determined by unpaired, two-tailed *t* test. (G) Actin (phalloidin), E-cad, and nuclei (Hoechst) localization in *Sun2*$^{-/-}$ MKCs in high Ca^{2+} medium for 24 h treated with the indicated drug for 5 h. Diagrams illustrate the effect of drug treatment on nuclear position. (H) Plots of nuclear centroid to cell centroid distance normalized to cell radius. Latrunculin A partially rescued the excessive nuclear movement of *Sun2*$^{-/-}$ MKCs. $n > 50$ cells (representative of three experiments). Asterisks denote indicated significance (**, $P = 0.0087$; ANOVA with Dunnett's posttest). The bottom and top of the box display the 25th and 75th percentiles, whereas the central band represents the median. The whiskers indicate the minimum and maximum values, and the plus signs indicate the mean. AU, arbitrary unit; cal, calcium; Blebb, blebbistatin; Lat A, Latrunculin A.

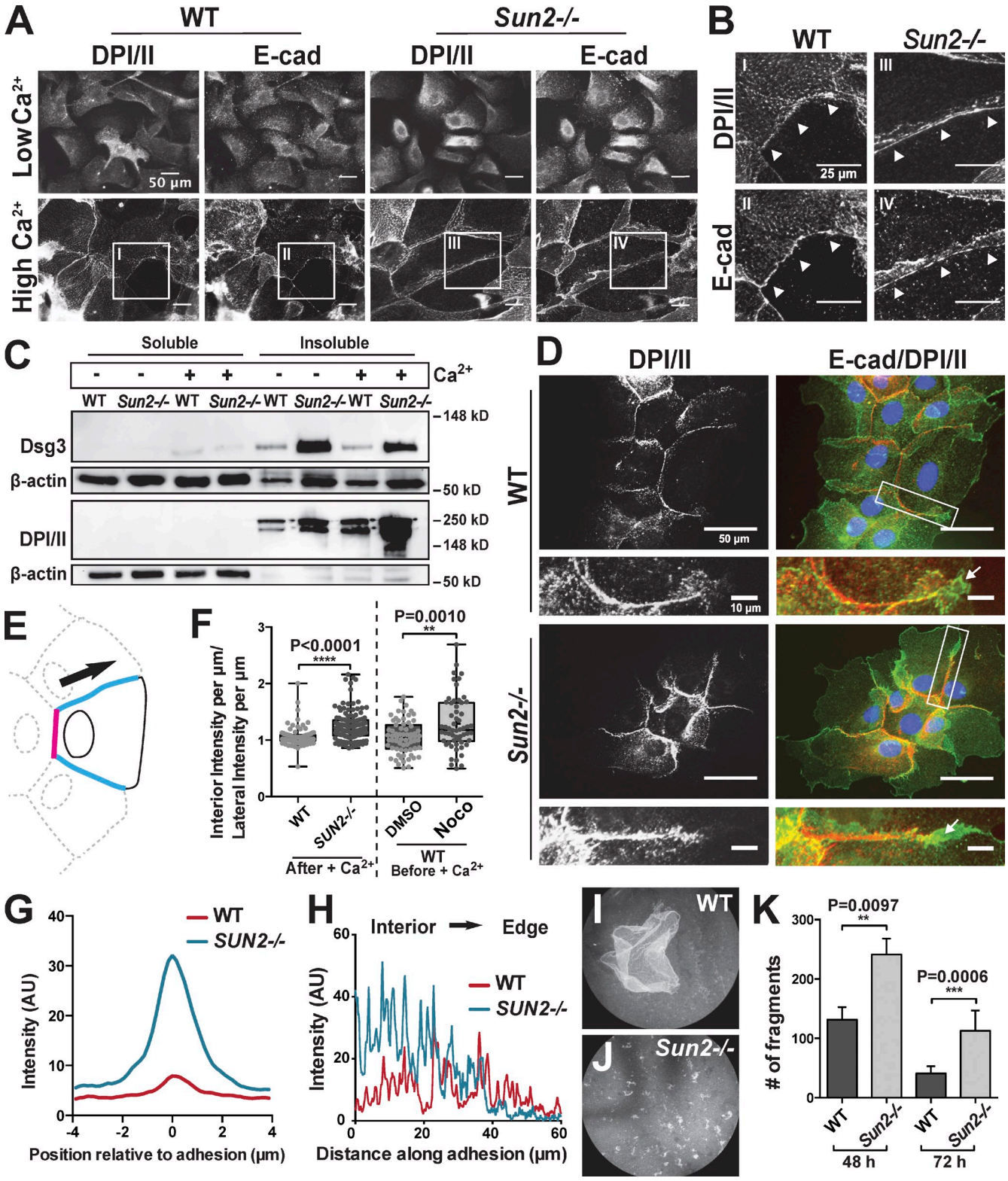

Figure 5. **Cultured *Sun2*$^{-/-}$ keratinocytes form altered, mechanically weak intercellular adhesions.** (A and B) WT or *Sun2*$^{-/-}$ MKCs in high Ca^{2+} medium after 72 h revealed desmosome (DPI/II) and AJ (E-cad) formation. (B) Insets from A show adhesion formation in WT and *Sun2*$^{-/-}$ MKCs (arrowheads). (C) Western blot analysis of Triton X-100–soluble and –insoluble fractions of WT and *Sun2*$^{-/-}$ MKC cell lysates, cultured in low or high Ca^{2+} medium, and probed for desmoglein 3 (Dsg3), desmoplakin I/II (DPI/II), and β-actin (loading control). (D) DPI/II (red), E-cad (green), and nuclear (Hoechst) localization in WT and *Sun2*$^{-/-}$ MKCs after 24 h in high Ca^{2+} medium revealed a uniform distribution of DPI/II along interior and lateral junctions in WT cells. This pattern of localization was perturbed in *Sun2*$^{-/-}$ cells. Insets display single lateral adhesions indicated by white boxes. (E) Diagram illustrating the location of interior (magenta) and lateral (blue) cell–cell adhesions in MKCs at the edge of colonies. Black arrow indicates direction of measurements in H. (F) The ratio of interior junction DPI/II intensity per micrometer to lateral junction DPI/II intensity per micrometer in WT and *Sun2*$^{-/-}$ MKCs after 24 h in high Ca^{2+} medium or for WT cells pretreated with DMSO or nocodazole before Ca^{2+} addition. Both *Sun2*$^{-/-}$ and nocodazole-treated MKCs displayed a significantly

We next asked whether perturbations in cytoskeletal organization could be responsible for the nuclear positioning defect in *Sun2*$^{-/-}$ MKCs. Inhibition of actomyosin contractility in *Sun2*$^{-/-}$ MKCs with blebbistatin after adhesion formation was unable to rescue the defective nuclear positioning (Fig. 4, G and H). However, depolymerization of the actin cytoskeleton with latrunculin A after adhesion formation could partially restore nuclear position in *Sun2*$^{-/-}$ MKCs to a more central, WT-like position (Fig. 4, G and H). Collectively, with the antagonistic roles for actin and MTs on nuclear position (Fig. 3) and the organization of MTs in *Sun2*$^{-/-}$ MKCs, these results suggest that the altered nuclear position in *Sun2*$^{-/-}$ MKCs reflects altered cytoskeletal dynamics. Furthermore, as complete depolymerization of the MT cytoskeleton in WT MKCs caused more severe nuclear positioning defects than in *Sun2*$^{-/-}$ MKCs, different pools of MTs with discrete functions may be disrupted upon loss of SUN2.

Desmosome distribution and adhesion strength are disrupted in *Sun2*$^{-/-}$ MKCs

Given the importance of MTs in the formation and function of intercellular adhesions (Pasdar et al., 1991; Nekrasova et al., 2011; Sumigray et al., 2011), we next examined AJ and desmosome formation in *Sun2*$^{-/-}$ MKCs. Cadherin-based AJs, marked by E-cad, did not differ greatly between WT and *Sun2*$^{-/-}$ MKCs, except for increased membrane overlap and ruffling in *Sun2*$^{-/-}$ cells (Figs. 2 G and 5, A and B, arrowheads). Likewise, desmosome formation appeared similar in WT and *Sun2*$^{-/-}$ MKCs as assessed by desmoplakin I/II (DPI/II) staining (Fig. 5, A and B, arrowheads; and Fig. S3 A).

Furthermore, *Sun2*$^{-/-}$ MKCs appeared competent to build desmosomes when assessed by biochemical fractionation, incorporating both desmoglein 3 (Dsg3) and DPI/II into the insoluble fraction of lysates after Ca^{2+} addition (Fig. 5 C). Indeed, *Sun2*$^{-/-}$ MKCs displayed elevated levels of incorporated Dsg3 and DPI/II. A similar up-regulation of classical and desmosomal cadherins has previously been observed in response to E-cad loss (Tunggal et al., 2005). We did note, however, apparent differences in the distribution of desmosomes (Fig. 5 D). In WT MKCs, DPI/II and E-cad appeared to distribute equally across both interior (Fig. 5 E, magenta) and lateral (Fig. 5 E, blue) junctions (Fig. 5 D, insets, arrows). In *Sun2*$^{-/-}$ MKCs, however, there was an increase in DPI/II staining at interior junctions (Fig. 5 D) and a depletion at lateral junctions, particularly near the free edge (Fig. 5 D, insets, arrows). To quantify this, we measured the ratio of DPI/II fluorescence at interior compared with lateral junctions as the intensity per micrometer for WT and *Sun2*$^{-/-}$ MKCs located at the colony edge and found an increased ratio of interior/lateral DPI/II intensity in *Sun2*$^{-/-}$ MKCs (Fig. 5 F). We further examined this effect by measuring the absolute intensity of DPI/II orthogonally across interior junctions and found a dramatic increase in *Sun2*$^{-/-}$ compared with WT MKCs (Fig. 5 G). Thus, desmosomes were preferentially assembled, or inadequately turned over, at interior cell–cell interfaces in the absence of SUN2.

Knowing that MT organization was perturbed in *Sun2*$^{-/-}$ MKCs, we next asked whether MT disruption during adhesion formation was sufficient to induce alterations in desmosome distribution. We treated WT MKCs with nocodazole before Ca^{2+} addition and analyzed the localization of DPI/II to interior and lateral adhesions after adhesion induction. Again, the ratio of interior/lateral DPI/II intensity was significantly greater in nocodazole-treated MKCs than DMSO-treated MKCs (Figs. 5 F and S3 B), suggesting that altered MT dynamics in *Sun2*$^{-/-}$ MKCs may be sufficient to produce the observed defects in desmosome distribution.

Because the interior/lateral ratio measurement integrates DPI/II staining along the entire lateral surface, we next evaluated line scans of DPI/II intensity along the representative lateral junctions in the insets in Fig. 5 D (Fig. 5 E, arrow). Although DPI/II was uniformly distributed along lateral adhesions in WT MKCs (Fig. 5 H, red), this staining was increased near interior adhesions and nearly lost at the colony-free edge in *Sun2*$^{-/-}$ MKCs (Fig. 5 H, blue). Indeed, a large proportion of *Sun2*$^{-/-}$ cells exhibited a loss of DPI/II staining proximal to colony edges (Fig. S3 C). These results further suggest that SUN2 is required to maintain proper adhesion targeting and/or turnover in MKCs.

To determine whether the defects in desmosome distribution seen in *Sun2*$^{-/-}$ MKCs influenced the strength of intercellular adhesion, we mechanically challenged adhesive monolayers of WT and *Sun2*$^{-/-}$ cells after 48 or 72 h in high Ca^{2+} medium (Huen et al., 2002). At both time points, sheets of *Sun2*$^{-/-}$ MKCs formed significantly more fragments when mechanically challenged than WT cells (Fig. 5, I–K). Given that *Sun2*$^{-/-}$ MKCs exhibit defects in desmosome distribution and cell–cell adhesion strength, we next considered whether these defects might underlie the hair follicle fragility seen in *Sun2*$^{-/-}$ mice.

Intercellular adhesions are defective in *Sun2*$^{-/-}$ hair follicles

Mice lacking the desmosomal cadherins Dsg3 or desmoglein 4 (Dsg4) exhibit alopecia after the first telogen, a defect attributed to abnormal intercellular trichocyte adhesion (Koch et al., 1998; Kljuic, et al., 2003). Together with the adhesion defects in

increased distribution of DPI/II at interior junctions. $n > 67$ cells per genotype and condition from three experiments. Statistical significance determined by unpaired, two-tailed *t* test. The bottom and top of the box display the 25th and 75th percentiles, whereas the central band represents the median. The whiskers indicate the minimum and maximum values, and the plus signs indicate the mean. (G) Averaged line scans of DPI/II intensity (arbitrary units [AU]) measured orthogonally across WT and *Sun2*$^{-/-}$ interior junctions for images as in D. $n > 26$ cells per genotype, three measurements per adhesion. (H) Line scans of DPI/II intensity (arbitrary units) along single representative WT and *Sun2*$^{-/-}$ MKC lateral adhesions, extending from the interior junctions to the cell edge (representative of $n > 106$ junctions from three experiments). (I and J) WT monolayers remained intact (I), whereas *Sun2*$^{-/-}$ monolayers fragmented drastically (J) after 72 h in high Ca^{2+} medium followed by mechanical challenge. (K) Quantification of the adhesion integrity assay in I and J. Error bars indicate SD for two replicates of three monolayers per genotype. Statistical significance determined by unpaired, two-tailed *t* test. AU, arbitrary unit; Noco, nocodazole.

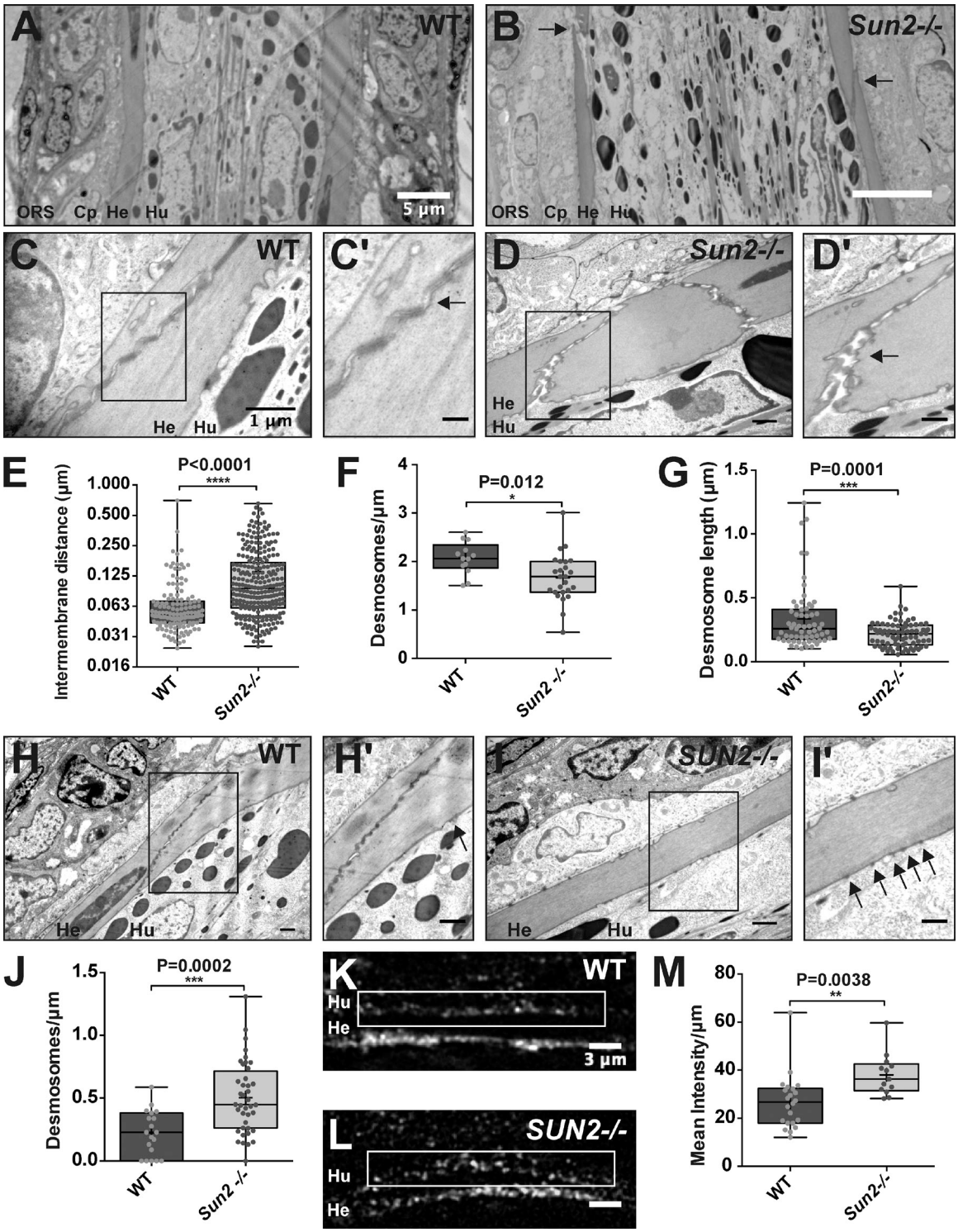

Figure 6. **Intercellular adhesions are structurally and functionally perturbed in *Sun2*$^{-/-}$ hair follicles.** Transmission electron micrographs of P4 WT and *Sun2*$^{-/-}$ follicles. (A and B) Overview of sectioned follicle structure, with the ORS at the edges of the image, followed by the companion (Cp), Henle (He), and Huxley (Hu) layers. Note the gaps between *Sun2*$^{-/-}$ He cells (B, arrows). (C and D) WT He–He cell junctions were evenly spaced with classical electron-dense desmosome morphology (C and C′, arrow), whereas *Sun2*$^{-/-}$ junctions included large gaps between cells, abnormal desmosome structure, and fewer desmosomes (D and D′, arrow). (E) Quantification of intermembrane spacings between He cells, displayed on a $\log_2$ scale. $n > 138$ adhesions from two mice. (F) Quantification of linear desmosome density between He layer cells. $n > 13$ cells from two mice. (G) Quantification of desmosome length between He layer cells. $n > 62$ desmosomes from two mice. (H and I) A greater number of desmosomes (insets H′ and I′, arrows) were found between He and Hu layer cells in *Sun2*$^{-/-}$ follicles. (J) Quantification of linear desmosome density between He and Hu cells. $n > 19$ cells from two mice. (K and L) Back skin from P4 WT and *Sun2*$^{-/-}$ mice immunostained for Dsg4. Junctions between He and Hu layers were desmosome rich (boxes). (M) Mean fluorescence intensity per micrometer for stretches of He–Hu junctions. $n > 13$ junctions. In all cases, statistical significance was determined by unpaired, two-tailed *t* test. For box and whiskers plots, the bottom and top of the box display the 25th and 75th percentiles, whereas the central band represents the median. The whiskers indicate the minimum and maximum values, and the plus signs indicate the means.

Sun2$^{-/-}$ MKCs, these data led us to hypothesize that adhesion could be disrupted in the hair follicles of *Sun2*$^{-/-}$ mice. To test this, we analyzed adhesions in P4 WT and *Sun2*$^{-/-}$ murine hair follicles using transmission EM (TEM). Although *Sun2*$^{-/-}$ follicles were grossly normal (Fig. 6, A and B), cells in the Henle (He) layer of the inner root sheath (IRS) displayed defects in adhesion, including widened intermembrane spaces (Fig. 6, B [arrows], C–D′ [arrows], and E). Consistent with this increased spacing, the desmosome density and desmosome length between He layer cells, identified by their electron-dense membrane-associated plaques, was significantly reduced in *Sun2*$^{-/-}$ follicles (Fig. 6, D′, F, and G).

Interestingly, the desmosome density between He and Huxley (Hu) layer cells was significantly increased in *Sun2*$^{-/-}$ follicles relative to WT (Fig. 6, H–I′ [arrows] and J). To corroborate these measurements, we immunostained skin sections for Dsg4 and measured the mean fluorescence intensity per micrometer along He–Hu layer boundaries defined by WGA staining (Fig. 6, K and L; and Fig. S4 A). We again found a greater desmosome density between He and Hu layer cells in *Sun2*$^{-/-}$ follicles (Fig. 6 M). In contrast, we did not observe any differences in hemidesmosome number or length in ORS cells (Fig. S4, B and C). Thus, the altered desmosome distribution in cultured *Sun2*$^{-/-}$ MKCs appears to be recapitulated in the hair follicle, particularly in the He and Hu layers. Furthermore, this change in desmosome distribution is once again linked to a failure of intercellular adhesion, in this case along the junctions between He cells in vivo.

SUN1 is up-regulated in the *Sun2*$^{-/-}$ epidermis during the second hair cycle

SUN1 and SUN2 are thought to be functionally redundant in most tissues (Crisp et al., 2006; Lei et al., 2009). We therefore hypothesized that the recovery of normal hair growth and follicle structure observed in *Sun2*$^{-/-}$ mice might occur as a result of an increase in SUN1 expression after the first hair cycle. We performed real-time PCR to quantify the levels of *Sun1* mRNA in isolated hair follicles of WT and *Sun2*$^{-/-}$ mice at P4 and P27. In *Sun2*$^{-/-}$ mice, *Sun1* mRNA levels were increased 2.5-fold at P27 compared with WT (Fig. S5 A). Furthermore, although minimal follicle-specific SUN1 staining was observed at P4 (Fig. 1 A), we observed increased NE-associated SUN1 expression in regenerated P32 hair follicles, particularly in *Sun2*$^{-/-}$ mice (Fig. S5 B, arrows). Although the SUN1 antibody produced high background staining (Fig. S5 C), specific staining—denoted by puncta at the nuclear rim—was observed in the basal and suprabasal layers of the epidermis, and in the IRS and ORS of P32 follicles (Figs. 1 A and S5 B, arrows). These data suggest that a compensatory increase in SUN1 expression after the first hair cycle may restore normal hair follicle structure in *Sun2*$^{-/-}$ mice by functionally regenerating LINC complexes. However, the defects in *Sun2*$^{-/-}$ MKCs, which express SUN1, suggest that either SUN1 can only partially compensate for SUN2, and this is sufficient for epidermal structure in vivo, and/or SUN1 up-regulation, which is not observed in *Sun2*$^{-/-}$ MKCs (Fig. S2 A), is necessary to support normal hair follicle structure.

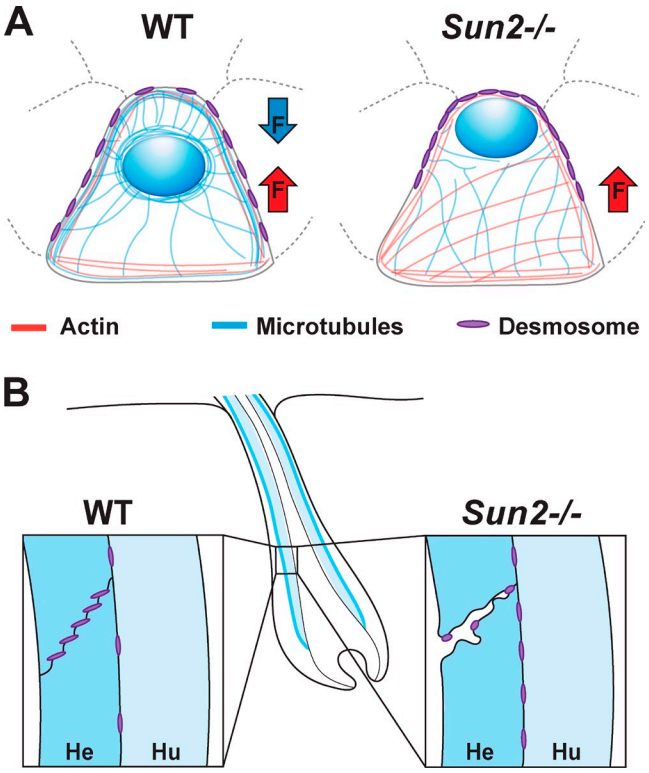

Figure 7. **Model of the effect of *Sun2* loss on intercellular adhesion and cytoskeletal organization in vitro and in vivo.** (A) Diagram depicting the organization of cytoskeletal elements, forces on nuclei (F in arrows), and desmosome distribution in differentiated WT and *Sun2*$^{-/-}$ MKCs. In WT cells, the MT and actin cytoskeletons appear to impose opposing forces on the nucleus, resulting in a bias in nuclear position toward interior adhesions. *Sun2*$^{-/-}$ cells display defective MT and actin organization; alterations in MT dynamics in *Sun2*$^{-/-}$ cells most likely produce the observed defect in nuclear positioning. An even distribution of desmosomes along interior and lateral intercellular adhesions is disrupted in *Sun2*$^{-/-}$ cells. (B) *Sun2*$^{-/-}$ hair follicles exhibit a desmosome deficiency along lateral-like He–He junctions, along with alterations in desmosome morphology and intermembrane spacing, as well as an increase in desmosomes along interior-like He–Hu junctions compared with WT follicles. These changes in desmosome density parallel the changes in desmosome distribution observed in vitro.

Discussion

In this study, we have identified a previously unappreciated role for the LINC complex component SUN2, and therefore the nuclear–cytoskeletal interface, in epithelial tissue integrity. Based on our data, we propose that the association of the cytoskeleton with the nucleus is central to both cytoskeletal and cell–cell adhesion organization and function (Fig. 7 A). By disrupting MTs and F-actin in WT MKCs, we are able to modulate nuclear positioning during adhesion formation, suggesting that the nucleus balances normally opposing forces provided by the actin and MT cytoskeletons (Fig. 7 A). We find that during intercellular adhesion formation, MKCs lacking SUN2 fail to correctly reorganize their MT cytoskeleton; we link this cytoskeletal defect to altered nuclear positioning. Furthermore, reorganization of the MT cytoskeleton after adhesion formation appears to be important for proper desmosome distribution, which in turn likely supports the mechanical strength of intercellular adhesion in vitro and in vivo.

The ability of the LINC complex to influence all elements of the cytoskeleton, and the resulting complexity of downstream effects, presents an ongoing challenge. LINC complex disruption can perturb the perinuclear organization of vimentin, keratin, and actin in various cell types (Lombardi et al., 2011; Postel et al., 2011; Rashmi et al., 2012; Chambliss et al., 2013). Our data suggest that SUN2 is particularly important for MT organization in adhesive MKCs, which could not only influence desmosome stability (Nekrasova et al., 2011; Sumigray et al., 2011; Sumigray and Lechler, 2011) but may also regulate actin-associated structures such as focal adhesions (Wu et al., 2008). Furthermore, although our data suggest that both actin and MTs impact nuclear positioning in MKCs, it is not clear how these cytoskeletal elements are coordinated in MKCs. Our observation that actomyosin contractility is initially required to drive nuclear movement toward intercellular adhesions in MKCs mirrors related processes in other contexts. Contractility aids in nuclear positioning during neuronal development (Bellion et al., 2005; Norden et al., 2009; Martini and Valdeolmillos, 2010; Strzyz et al., 2015), whereas myosin-dependent retrograde actin flow, coupled to transmembrane actin-associated lines, drives the nucleus rearward in fibroblasts (Gomes et al., 2005; Luxton et al., 2010). MTs also influence nuclear position and interface with the LINC complex through the molecular motors dynein and kinesin (Malone et al., 2003; Fridolfsson et al., 2010; Yu et al., 2011), although polymerization-derived pushing forces have also been implicated in nuclear movement (Zhao et al., 2012). Further work will be required to define the mechanisms by which the cytoskeleton positions nuclei in response to adhesion formation in MKCs. In addition, a role for keratin in positioning the nucleus and influencing desmosome distribution in MKCs cannot be ruled out. Recent work indicates that vimentin intermediate filaments are trafficked to the cell cortex in an MT-dependent fashion (Hookway et al., 2015), suggesting that the *Sun2*$^{-/-}$ phenotype may be attributed to keratin dysfunction downstream of MT disorganization. Importantly, our observation that MT depolymerization is sufficient to recapitulate the *Sun2*$^{-/-}$ MKC nuclear positioning and desmosome distribution defects indicates that MT organization plays an important role in intercellular adhesion.

Our study provides evidence that the ability of the nucleus to integrate mechanical inputs from cytoskeletal elements may control the balance of cellular tension in MKCs. SUN2 specifically seems to allow MTs to counterbalance forces generated by the actin cytoskeleton (Fig. 7 A). Although the LINC complex has been implicated in nuclear positioning by mediating nuclear–cytoskeletal force transmission (Lombardi and Lammerding, 2011), the adhesion-dependent nuclear movement in MKCs suggests that nuclei are responsive to tension at cell–cell junctions. This role of the nucleus could prove critical to the mechanical robustness of intercellular adhesions, which both modulate and respond to changes in cytoskeletal tension (le Duc et al., 2010; Yonemura et al., 2010; Borghi et al., 2012; Ray et al., 2013; Harris et al., 2014), and, ultimately, tissue homeostasis. Tension is coordinated across multiple cells through AJs (Mertz et al., 2013), and the integrity of cohesive epithelial cells is regulated by the distribution of tension at apical versus lateral AJs (Wu et al., 2014). Thus, the potential function of the nucleus to regulate cellular tension could strongly influence adhesion.

MTs can contact and cluster cadherin proteins and are required for maintaining adhesions and generating polarity in epithelial cells (Siegrist and Doe, 2007). We find a SUN2-dependent polarity of desmosome localization to interior and lateral junctions of both MKCs in vitro and in hair follicle trichocytes in vivo (Fig. 7, A and B). Indeed, the desmosome deficiency in lateral He–He junctions and enrichment in interior He–Hu junctions of *Sun2*$^{-/-}$ mice closely mimics our in vitro observations (Fig. 7 B). Interestingly, companion–He junctions contain scant desmosomes compared with He–He junctions, somewhat recapitulating the organization of adhesions in MKC colonies (Morioka, 2005). Given the importance of the MT cytoskeleton in desmosome targeting (Nekrasova et al., 2011), the defects in desmosome distribution in *Sun2*$^{-/-}$ MKCs may result from alterations in MT organization that influence the adhesion-dependent reorganization of centrosomal components, such as Lis1, which are crucial for cortical MT stabilization (Sumigray et al., 2011; Sumigray and Lechler, 2011). Alternatively, the close apposition of nuclei with interior junctions could result in defects in cadherin targeting, migration, or internalization (Kametani and Takeichi, 2007; Niessen et al., 2011; Wang et al., 2012). It remains unclear whether the nuclear positioning defect in *Sun2*$^{-/-}$ MKCs simply reflects the altered cytoskeletal organization observed in these cells or whether it directly influences desmosome localization. Further studies will be required to dissect these questions.

The compromised adhesion between He cells in *Sun2*$^{-/-}$ hair follicles supports the hypothesis that the force of hair growth generates a slippage plane that exerts force on He–He junctions, as the hair shaft and its associated IRS move toward the skin's surface (Stenn and Paus, 2001). Interestingly, the defects in *Sun2*$^{-/-}$ hair follicle structure are reminiscent of the hair follicles of patients with loose anagen hair syndrome, characterized by easily pluckable hairs with defective He and Hu structures, which often resolves as individuals age into adulthood (Mirmirani et al., 2011). Whether LINC complex components are altered in loose anagen hair syndrome or other skin disorders in which intercellular adhesions and epithelial tissue integrity are affected will be an interesting area of future study.

Materials and methods

Mouse breeding and care

All animal care and experimental procedures were conducted in accord with requirements approved by the Institutional Animal Care and Use Committee of Yale University. *Sun1*$^{-/-}$ (strain B6;129S6-*Sun1*^{tm1Mhan}/J), *Sun2*$^{-/-}$ (strain B6;129S6-*Sun2*^{tm1Mhan}/J), and C57BL/6 WT mice were obtained from Jackson ImmunoResearch Laboratories, Inc. *Sun1*$^{-/-}$ mice were previously generated through the replacement of exons 10–13 with a neomycin resistance cassette (Ding et al., 2007), whereas *Sun2*$^{-/-}$ mice were generated through the replacement of exons 11–16 and part of exon 17 with a neomycin resistance cassette (Lei et al., 2009).

Isolation and culture of primary mouse keratinocytes

Mouse keratinocytes were isolated from skin from newborn *Sun2*$^{-/-}$ or WT pups as previously described (Mertz et al., 2013). Under sterile conditions,

pups were sacrificed, and back skin was excised, washed in PBS, and floated on dispase at 4°C for 16–20 h. Epidermis was separated from the dermis with forceps and incubated in 0.25% trypsin for 15 min at RT. Cells were liberated by trituration, filtered using a 40–70-µm strainer, and plated on mitomycin-C–treated J2 fibroblasts in medium-calcium medium (0.3 mM $CaCl_2$). After two to four passages, keratinocytes were plated on plastic dishes without feeder cells and maintained in media containing 0.05 mM $CaCl_2$ (E-low calcium media).

Mouse tissue isolation, histology, and immunofluorescence staining

Frozen back skin samples embedded in O.C.T. compound (Tissue-Tek) were sectioned using a cryostat (CM3050S; Leica). For histological analyses, 10-µm sections were cut and stained with hematoxylin and eosin. For immunofluorescence, 6- or 8-µm sections were fixed in 4% formaldehyde at RT for 10 min. For immunostaining with nonmouse primary antibodies, tissue sections were blocked in gelatin block (2.5% normal goat serum, 1% BSA, 2% gelatin, and 0.25% Triton X-100 in PBS) at RT for 1 h and incubated with the following primary antibodies overnight at 4°C: SUN2 (1:1,000; rabbit; ab124916; Abcam), SUN1 (1:1,000; rabbit; ab124770; Abcam), α_6 integrin (1:500; rat; GoH3; R&D Systems), keratin 6 (1:100; rabbit; Covance), and E-cad (1:200; rat; DECMA-1; Abcam). Sections were subsequently washed in multiple changes of PBS and incubated with fluorescent dye–conjugated secondary antibodies (1:2,000; mouse, rat, or rabbit; Alexa Fluor; Life Technologies). Costaining with Hoechst 33342 (Thermo Fisher Scientific) diluted in PBS (1:2,000) or Alexa Fluor 488–conjugated WGA (Life Technologies) diluted in PBS (1:2,000) was performed when indicated. Sections were mounted using Fluoromount-G mounting medium (SouthernBiotech). For immunostaining with the mouse primary antibodies AE15 (1:500; mouse; sc-80607; Santa Cruz Biotechnology, Inc.) and Dsg4 (1:50; mouse; 18G8; against the intracellular domain; Bazzi et al., 2006), the Mouse-on-Mouse Immunodetection kit Blocking Reagent and Protein Diluent (Vector Laboratories) were used according to manufacturer's instructions.

For immunostaining of cells on coverslips, cells were fixed in 4% paraformaldehyde for 10 min at RT and washed with PBS. Cells were then permeabilized in 0.5% Triton X-100 in PBS at RT for 10 min, blocked using 10% goat serum, 5% BSA, and 0.5% Tween 20 in PBS for 1 h, and subsequently incubated with primary antibody diluted in blocking buffer at 37°C for 1 h. In addition to the primary antibodies in the previous paragraph, DP I/II (1:200; mouse; Abcam), β-tubulin (1:60; mouse; TUB 2.1; Sigma-Aldrich), phospho–myosin light chain (1:200; mouse; Cell Signaling Technology), and K14 (1:1,000; goat; custom against the C-terminal sequence [KVVSTHEQVLRTKN] through New England Peptide) were used in immunostaining cells. Coverslips were washed in PBS for 15 min and incubated with fluorescently conjugated secondary antibodies diluted in PBS (1:1,000) at RT for 1 h. Costaining with Hoechst 33342 (1:2,000; Thermo Fisher Scientific) or Alexa Fluor 594– or Alexa Fluor 647–conjugated phalloidin (1:40; Invitrogen) diluted in blocking buffer was performed when indicated. Coverslips were washed and mounted using Fluoromount-G.

Imaging and image analysis

Hematoxylin and eosin–stained skin sections were imaged on a microscope (Axio Imager M1) with AxioVision software (version 4.8.2.0) and a camera (AxioCam MRm; Carl Zeiss). Skin sections processed for immunofluorescence were imaged on a widefield deconvolution microscope (DeltaVision; Applied Precision/GE Healthcare) with a charge-coupled device (CCD) camera (CoolSNAP K4; Photometrics) and SoftWoRx software or a microscope (Axio Imager Z1; Carl Zeiss) with a CCD camera (ORCA-ER; Hamamatsu Photonics) and AxioVision software (version 4.8.2.0). Immunocytochemistry images were captured using the described Axio Imager Z1, Axio Imager M1, and DeltaVision microscopes. Specifically, images in Figs. 1 D, 3 (B and F), S1 G, and S2 (B and D) were acquired on the Axio Imager M1. Images in Figs. 1 (A, B, F, and G), 2 (A–D, F, and G), 3 (B and F), 4 (E and G), 5 (A, B, and D), S1 (E and F), and S3 (A–C) were acquired on the Axio Imager Z1. Images in Figs. 4 (A–C), S1 (A–D, H, and I), S2 F, S4 A, and S5 (B and C) were acquired on the DeltaVision microscope. All images acquired on the DeltaVision microscope were deconvolved using the Deconvolve tool (constrained iterative deconvolution) in SoftWoRx software. The DeltaVision microscope was equipped with an oil Plan Apochromat N 60×/1.42 NA objective (Olympus). The Axio Imager Z1 microscope was equipped with air EC Plan Neofluar 10×/0.3 Ph1 (Carl Zeiss), air Plan Apochromat 20×/0.8 NA (Carl Zeiss), and oil EC Plan Neofluar 40×/1.30 NA objectives (Carl Zeiss). The Axio Imager M1 was equipped with air EC Plan Neofluar 10×/0.3 NA (Carl Zeiss), air Plan-Apochromat 20×/0.8 NA (Carl Zeiss), and oil EC Plan Neofluar 40×/1.3 NA objectives (Carl Zeiss). In all cases, images were analyzed using Fiji software (ImageJ 1.48d; National Institutes of Health) as indicated.

For the analysis of follicular bending at P4, fluorescent images of K6 staining were acquired on the Axio Imager Z1 using the 20× objective, and follicles were counted as bent if they contained at least one bend <130°, which corresponded to a severe deviation from normal follicle structure; this analysis was performed for three mice. Angles were measured in Fiji using the angle tool.

Images for nuclear positioning assays were acquired either on the Axio Imager Z1 or Axio Imager M1 using the 20× objectives. Nuclear-to-cell centroid distance was calculated as $(\text{cell centroid} - \text{nucleus centroid})/\sqrt{\text{cell area}}$; normalization to cell area was performed as a result of variability in cell size. For Figs. 2 H and 3 C, statistical significance was determined using unpaired, two-tailed *t* tests with Prism software (version 6; GraphPad Software), with Welch's correction when appropriate. For Figs. 3 G, 4 H, S2 (C and E), statistical significance was determined by analysis of variance (ANOVA) with Dunnett's multiple comparisons posttest with Prism; for Figs. 2 E and 3 (D and H), it was determined by ANOVA with Tukey's multiple comparisons posttest with Prism. For box and whiskers plots, the bottom and top of the box display the 25th and 75th percentiles, whereas the central band represents the median. The whiskers indicate the minimum and maximum values, and the plus signs indicate the mean.

For cortical MT organization analyses, images were acquired on the Axio Imager Z1 with the 40× objective, and cells were considered to have a cortical accumulation of MTs if β-tubulin staining at the cell periphery was observed to run parallel to the cell surface. Statistical significance was determined by ANOVA with Dunnett's posttest with Prism. Because the quantitative analysis of perinuclear MTs and K14 in *Sun2*$^{-/-}$ MKCs proved technically challenging as a result of the close proximity of nuclei and adhesions in these cells, a qualitative assessment of perinuclear β-tubulin and K14 was made, as indicated in the Results. For the analysis of NE-associated MTs in taxol-treated cells, images were acquired on the Axio Imager Z1 with the 20× objective, and cells were counted as positive for NE-associated MTs only if an unbroken ring of β-tubulin staining, surrounding the Hoechst signal, was observed (see Fig. 4 E, image III for a cell positive for this MT organization). In all other cases, cells were scored as negative for NE-associated MTs.

For the analysis of desmosome distribution, images were acquired on the Axio Imager Z1 with the 40× objective, and only cells with one free edge, at least three cell–cell contacts, and two visible lateral junctions were measured. Interior and lateral junctions were identified by both DPI/II and E-cad staining. The plot profiles corresponding to the fluorescence intensity of DPI/II per micrometer for interior and lateral junctions were measured, the intensity per micrometer for each junction was determined, and the ratio of interior DPI/II intensity per micrometer to lateral DPI/II intensity per micrometer was calculated. For the analysis of DPI/II fluorescence intensity at interior junctions, images were background subtracted in Fiji with a rolling ball radius of 200 pixels. 8-µm lines centered on each interior junction were drawn orthogonally across junctions, and the DPI/II plot profile was measured for at least three regions per junction. The plot profile values were then averaged across the 8-µm segments for each genotype. Line scan analyses of DPI/II fluorescence intensity along lateral junctions were performed for the representative junctions indicated in Fig. 5 D (insets). The beginnings of lateral junctions were defined as the intersection between interior and lateral junctions, whereas the cell-free edges were defined by a loss of E-cad staining. Images were background subtracted in Fiji with a rolling ball radius of 200 pixels, and DPI/II fluorescence intensity line scans were collected. For the quantification of DPI/II localization to lateral junction edges, junctions were considered positive for DPI/II staining at junction edges if any DPI/II staining was observed above the background signal at the free edge. For the immunofluorescence desmosome density analysis of skin sections, images were acquired on the DeltaVision widefield deconvolution microscope with the 60× objective, deconvolved, and background subtracted in Fiji. He layer and Hu layer cell–cell junctions were identified based on WGA staining and nuclear shape. The plot profile corresponding to the fluorescence intensity along cell–cell junctions was measured, and the mean fluorescence intensity per micrometer was calculated; this analysis was performed for one mouse. Unless otherwise stated, statistical significance was determined by unpaired, two-tailed *t* tests with Prism software.

Intercellular adhesion and cell integrity assays

For adhesion formation assays, low passage MKCs were trypsinized using 0.25% trypsin–EDTA (Life Technologies), seeded on 18-mm glass coverslips coated in 50 µg/ml fibronectin (Sigma-Aldrich) in 12-well dishes, and allowed to adhere in E-low calcium medium for 16 h. Once small colonies

had formed, cells were washed with PBS and incubated in 1.2 mM calcium-containing medium to induce cell junction assembly. Cells were washed and fixed in 4% paraformaldehyde in PBS for 10 min at RT at 0, 24, 48, and 72 h after calcium addition, and processed for immunofluorescence staining. For nuclear positioning assays, cells were fixed at 0, 6, 12, and 24 h after calcium addition (see Mouse tissue isolation, histology, and immunofluorescence staining). For intercellular adhesion integrity assays, WT and *Sun2*$^{-/-}$ cells were seeded in three wells each of 6-well plates and grown in E-low calcium media for 24 h to 100% confluency. Cells were switched to high calcium media to induce adhesion formation and incubated for 48 or 72 h. Monolayers were washed twice in PBS + 1.2 mM $CaCl_2$ and incubated with 2.4 U/ml dispase II (Roche) for 30 min at 37°C. Once completely released from the bottoms of the wells, monolayers were carefully transferred to 15-ml conical tubes, washed three times in PBS + 1.2 mM $CaCl_2$, and then rotated 20× in a total volume of 5 ml PBS + 1.2 mM $CaCl_2$. Fragments were counted using a dissecting microscope (SZH Zoom Stereo Microscope; Olympus) at 7.5× magnification.

Cytoskeletal disruption with pharmacological agents

For the analysis of nuclear positioning in drug-treated WT MKCs, cells were trypsinized and allowed to adhere to 50 µg/ml fibronectin-coated glass coverslips in E-low calcium media for 16 h. For drug treatment before calcium addition (during adhesion formation), cells were incubated with DMSO vehicle, 10 µM blebbistatin, 10 µM Y-27632, 10 µM nocodazole, and 10 µM blebbistatin in combination with 10 µM nocodazole or 10 µM Y-27632 in combination with 10 µM nocodazole in low calcium media for 30 min at 37°C. Calcium was then added to a final concentration of 1.2 mM to induce adhesion formation, and the cells were incubated in high calcium media with a drug for an additional 6 h. The coverslips were then washed in PBS, fixed in 4% paraformaldehyde for 10 min at RT, and processed for immunofluorescence staining. Nuclear position was analyzed as described in Imaging and image analysis. For drug treatment after calcium addition, cells were exposed to 1.2 mM calcium-containing media for 24 h. DMSO vehicle, 10 µM blebbistatin, 10 µM Y-27632, 0.5 µM latrunculin A, 10 µM nocodazole, and 10 µM blebbistatin in combination with 10 µM nocodazole or 10 µM Y-27632 in combination with 10 µM nocodazole were then added to the cells for an additional 5 h. Cells treated with drug after calcium addition were fixed, processed, and analyzed in the same manner as cells treated before calcium addition. For the analysis of taxol-stabilized MTs in WT MKCs, cells were prepared for drug treatment in the same manner as cells treated with drug after calcium addition and incubated with 1.2 mM calcium-containing media for 24 h. 10 µM taxol was then incubated with the cells for an additional 5 h, and the coverslips were processed for immunofluorescence staining. For the analysis of nuclear position in drug-treated *Sun2*$^{-/-}$ MKCs, cells were prepared for drug treatment in the same way as WT cells and then incubated with 1.2 mM calcium-containing media for 24 h. DMSO vehicle, 10 µM blebbistatin, or 0.5 µM latrunculin A was then incubated with cells for an additional 5 h before coverslips were processed for immunofluorescence staining as in Mouse tissue isolation, histology, and immunofluorescence staining and analyzed as in Imaging and image analysis.

Western blot analysis

Whole-cell lysates of WT and *Sun2*$^{-/-}$ MKCs were prepared on ice in radioimmunoprecipitation lysis buffer (50 mM Tris-Cl, pH 7.4, 1 mM EDTA, 1% NP-40 alternative, 0.1% Na deoxycholate, 0.1% SDS, 150 mM NaCl, and protease inhibitor cocktail [Sigma-Aldrich]). The insoluble debris was removed by centrifugation for 20 min at 14,000 rpm in a 4°C tabletop microcentrifuge (Sorvall Legend Micro 21R; Thermo Fisher Scientific). The supernatant was stored at −80°C for later use. Extracted protein samples were diluted in SDS-PAGE sample buffer and separated using a 7.5% polyacrylamide gel. The separated proteins were transferred to a nitrocellulose membrane using a transfer system (Bio-Rad Laboratories). Membranes were subsequently blocked in 10% nonfat milk (Omniblok; American Bioanalytical) in TBST (TBS with Tween 20) for 1 h at RT and incubated with SUN1 (1:1,000; rabbit; Epitomics), SUN2 (1:1,000; rabbit; Abcam), or β-actin (1:1,000; mouse; Abcam) primary antibodies at 4°C overnight. The membranes were washed for 15 min in TBST and then incubated for 1 h with HRP-conjugated secondary antibodies (1:5,000; Pierce Antibodies; Thermo Fisher Scientific) in TBST at RT. After washes with TBST, the membranes were incubated with HRP chemiluminescent substrate (SuperSignal West Femto Chemiluminescent Substrate; Thermo Fisher Scientific) for 5 min and then imaged using an imaging system (VersaDoc; Bio-Rad Laboratories). For the analysis of desmosomal protein fractionation, whole cell lysates of WT and *Sun2*$^{-/-}$ MKCs were prepared on ice using Triton X-100 lysis buffer (10 mM Tris-Cl, pH 7.5, 5 mM EDTA, 1% Triton X-100, 145 mM NaCl, and protease inhibitor cocktail [Sigma-Aldrich]). Triton X-100–soluble and –insoluble fractions were isolated by centrifugation in the same manner as for lysates prepared with radioimmunoprecipitation assay buffer. The soluble supernatants were diluted in 2× SDS-PAGE sample buffer, the insoluble pellets were diluted in SDS-PAGE sample buffer containing 8 M urea, and the proteins were separated using a 7.5% polyacrylamide gel and transferred to nitrocellulose. Membranes were blocked in 10% milk in TBST for 1 h at RT and incubated with Dsg3 (1:500; goat; Santa Cruz Biotechnology, Inc.), DPI/II (1:500; mouse; Abcam), or β-actin (1:1,000; mouse; Abcam) primary antibodies at 4°C overnight. The membranes were then processed using the chemiluminescent substrate and the Bio-Rad imaging system.

TEM

TEM was performed in the Yale School of Medicine Center for Cellular and Molecular Imaging Electron Microscopy core facility. Back skin sections from P4 WT and *Sun2*$^{-/-}$ mice were isolated and processed for TEM; two mice were examined for each genotype. Tissue blocks were fixed in 2.5% glutaraldehyde/2% paraformaldehyde in 0.1 M sodium cacodylate buffer, pH 7.4, for 30 min at RT and 1.5 h at 4°C. The samples were rinsed in sodium cacodylate buffer and were postfixed in 1% osmium tetroxide for 1 h. The samples were rinsed and en bloc stained in aqueous 2% uranyl acetate for 1 h followed by rinsing, dehydrating in an ethanol series to 100%, rinsing in 100% propylene oxide, infiltrating with EMbed 812 (Electron Microscopy Sciences) resin, and baking overnight at 60°C. Hardened blocks were cut using an ultramicrotome (UltraCut UC7; Leica). Ultrathin 60-nm sections were collected and stained using 2% uranyl acetate and lead citrate for transmission microscopy. Carbon-coated grids were viewed on a transmission electron microscope (Tecnai BioTWIN; FEI) at 80 kV. Images were taken using a CCD camera (Morada; Olympus) and iTEM (Olympus) software.

Gene expression analysis

Real-time PCR was performed as previously described (Festa et al., 2011). In brief, total RNA was isolated with TRIzol (Invitrogen) and RNeasy kit (QIAGEN) from isolated hair follicles from P4–5 and P27 *Sun2*$^{-/-}$ or *WT* mice. To isolate hair follicles, dorsal (P4) or tail (P27) mouse skin was floated overnight on dispase (Gibco). The epidermis was removed by force, and the dermis was minced with scissors and incubated in collagenase 1a (Sigma-Aldrich) followed by trituration and low-speed centrifugation to isolate hair follicles. TRIzol was added to the purified hair follicles, and total RNA was isolated according to manufacturer's instructions. To generate cDNA, equal amounts of total RNA (1,000 ng) were added to reverse transcription reaction mix (Agilent Technologies) with oligo-dT as a primer. Quantitative real-time PCR was conducted with a LightCycler system (Roche) using the LightCycler DNA master SYBR Green kit for 45 cycles. Primers used in these experiments are SUN1 forward, 5′-CCACTTCTGGGGTCTCGATG-3′, and reverse, 5′-TGCAGTCACGGCAAGTGTAT-3′; and β-actin forward, 5′-ATCAAGATCATTGCTCCTCCTGAG-3′, and reverse, 5′-CTGCTTGCTGATCCACATCTG-3′. PCR product levels were normalized to β-actin mRNA levels.

Online supplemental material

Fig. S1 shows SUN2 localization in the hair follicle during the first hair cycle, SUN2 staining in *Sun2*$^{-/-}$ skin, *Sun1*$^{-/-}$ skin hematoxylin and eosin, and bends in the ORS of *Sun2*$^{-/-}$ hair follicles. Fig. S2 shows SUN2 and SUN1 Western blots of MKCs, additional images for the nuclear positioning assay quantifications in Fig. 2 E, nuclear positioning assays with Y-27632 treatment, and cytoskeletal organization in MKCs cultured in low Ca^{2+} medium. Fig. S3 shows additional images for the intercellular adhesion analyses in Fig. 5 A and the DPI/II localization analysis in nocodazole-treated MKCs for Fig. 5 F as well as the quantification of DPI/II at lateral junction free edges for Fig. 5 D. Fig. S4 shows additional images of Dsg4 and WGA costaining in skin for Fig. 6 (K and L), and the quantification of hemidesmosome length and number in hair follicles. Fig. S5 shows SUN1 gene expression analysis, and immunofluorescence images of hair follicles illustrating SUN1 staining at P32. Online supplemental material is available at http://www.jcb.org/cgi/content/full/jcb.201502024/DC1. Additional data are available in the JCB DataViewer at http://dx.doi.org/10.1083/jcb.201502024.dv.

We would like to thank Morven Graham for technical expertise and the King and Horsley laboratories for valuable comments on the manuscript.

This work was supported by a Searle Scholar Award and the G. Harold & Leila Y. Mathers Charitable Foundation (to M.C. King), a Dermatologist Investigator Research Fellowship (Dermatology Foundation; to A.E. Zubek), a Gruber Science Fellowship (to R.M. Stewart), and training grants T32-HD007180 (to K.A. Rosowski and R.M. Stewart) T32-GM007223 (to K.A. Rosowski), and Ruth L. Kirschstein National Research Service Award 5T32AR007016 (to A.E. Zubek). V. Horsley is a Pew Scholar in Biomedical Research and is funded by the National Institutes of Health (AR060295) and the Connecticut Department of Public Health (12SCBYALE01).

V. Horsley is a consultant and receives grant support from Unilever and Schick. The other authors declare no competing financial interests.

Submitted: 6 February 2015
Accepted: 6 April 2015

References

Bazzi, H., A. Getz, M.G. Mahoney, A. Ishida-Yamamoto, L. Langbein, J.K. Wahl III, and A.M. Christiano. 2006. Desmoglein 4 is expressed in highly differentiated keratinocytes and trichocytes in human epidermis and hair follicle. *Differentiation*. 74:129–140. http://dx.doi.org/10.1111/j.1432-0436.2006.00061.x

Bellion, A., J.P. Baudoin, C. Alvarez, M. Bornens, and C. Métin. 2005. Nucleokinesis in tangentially migrating neurons comprises two alternating phases: forward migration of the Golgi/centrosome associated with centrosome splitting and myosin contraction at the rear. *J. Neurosci.* 25:5691–5699. http://dx.doi.org/10.1523/JNEUROSCI.1030-05.2005

Borghi, N., M. Sorokina, O.G. Shcherbakova, W.I. Weis, B.L. Pruitt, W.J. Nelson, and A.R. Dunn. 2012. E-cadherin is under constitutive actomyosin-generated tension that is increased at cell-cell contacts upon externally applied stretch. *Proc. Natl. Acad. Sci. USA*. 109:12568–12573. http://dx.doi.org/10.1073/pnas.1204390109

Brosig, M., J. Ferralli, L. Gelman, M. Chiquet, and R. Chiquet-Ehrismann. 2010. Interfering with the connection between the nucleus and the cytoskeleton affects nuclear rotation, mechanotransduction and myogenesis. *Int. J. Biochem. Cell Biol.* 42:1717–1728. http://dx.doi.org/10.1016/j.biocel.2010.07.001

Chambliss, A.B., S.B. Khatau, N. Erdenberger, D.K. Robinson, D. Hodzic, G.D. Longmore, and D. Wirtz. 2013. The LINC-anchored actin cap connects the extracellular milieu to the nucleus for ultrafast mechanotransduction. *Sci Rep*. 3:1087. http://dx.doi.org/10.1038/srep01087

Crisp, M., Q. Liu, K. Roux, J.B. Rattner, C. Shanahan, B. Burke, P.D. Stahl, and D. Hodzic. 2006. Coupling of the nucleus and cytoplasm: Role of the LINC complex. *J. Cell Biol.* 172:41–53. http://dx.doi.org/10.1083/jcb.200509124

Dahl, K.N., A.J.S. Ribeiro, and J. Lammerding. 2008. Nuclear shape, mechanics, and mechanotransduction. *Circ. Res.* 102:1307–1318. http://dx.doi.org/10.1161/CIRCRESAHA.108.173989

Ding, X., R. Xu, J. Yu, T. Xu, Y. Zhuang, and M. Han. 2007. SUN1 is required for telomere attachment to nuclear envelope and gametogenesis in mice. *Dev. Cell*. 12:863–872. http://dx.doi.org/10.1016/j.devcel.2007.03.018

Dupin, I., E. Camand, and S. Etienne-Manneville. 2009. Classical cadherins control nucleus and centrosome position and cell polarity. *J. Cell Biol.* 185:779–786. http://dx.doi.org/10.1083/jcb.200812034

Engl, W., B. Arasi, L.L. Yap, J.P. Thiery, and V. Viasnoff. 2014. Actin dynamics modulate mechanosensitive immobilization of E-cadherin at adherens junctions. *Nat. Cell Biol.* 16:587–594. http://dx.doi.org/10.1038/ncb2973

Festa, E., J. Fretz, R. Berry, B. Schmidt, M. Rodeheffer, M. Horowitz, and V. Horsley. 2011. Adipocyte lineage cells contribute to the skin stem cell niche to drive hair cycling. *Cell*. 146:761–771. http://dx.doi.org/10.1016/j.cell.2011.07.019

Fridolfsson, H.N., N. Ly, M. Meyerzon, and D.A. Starr. 2010. UNC-83 coordinates kinesin-1 and dynein activities at the nuclear envelope during nuclear migration. *Dev. Biol.* 338:237–250. http://dx.doi.org/10.1016/j.ydbio.2009.12.004

Galbraith, C.G., K.M. Yamada, and M.P. Sheetz. 2002. The relationship between force and focal complex development. *J. Cell Biol.* 159:695–705. http://dx.doi.org/10.1083/jcb.200204153

Gardel, M.L., I.C. Schneider, Y. Aratyn-Schaus, and C.M. Waterman. 2010. Mechanical integration of actin and adhesion dynamics in cell migration. *Annu. Rev. Cell Dev. Biol.* 26:315–333. http://dx.doi.org/10.1146/annurev.cellbio.011209.122036

Gomes, E.R., S. Jani, and G.G. Gundersen. 2005. Nuclear movement regulated by Cdc42, MRCK, myosin, and actin flow establishes MTOC polarization in migrating cells. *Cell*. 121:451–463. http://dx.doi.org/10.1016/j.cell.2005.02.022

Grashoff, C., B.D. Hoffman, M.D. Brenner, R. Zhou, M. Parsons, M.T. Yang, M.A. McLean, S.G. Sligar, C.S. Chen, T. Ha, and M.A. Schwartz. 2010. Measuring mechanical tension across vinculin reveals regulation of focal adhesion dynamics. *Nature*. 466:263–266. http://dx.doi.org/10.1038/nature09198

Guilluy, C., L.D. Osborne, L. Van Landeghem, L. Sharek, R. Superfine, R. Garcia-Mata, and K. Burridge. 2014. Isolated nuclei adapt to force and reveal a mechanotransduction pathway in the nucleus. *Nat. Cell Biol.* 16:376–381. http://dx.doi.org/10.1038/ncb2927

Harris, T.J.C., and U. Tepass. 2010. Adherens junctions: from molecules to morphogenesis. *Nat. Rev. Mol. Cell Biol.* 11:502–514. http://dx.doi.org/10.1038/nrm2927

Harris, A.R., A. Daeden, and G.T. Charras. 2014. Formation of adherens junctions leads to the emergence of a tissue-level tension in epithelial monolayers. *J. Cell Sci.* 127:2507–2517. http://dx.doi.org/10.1242/jcs.142349

Hong, S., R.B. Troyanovsky, and S.M. Troyanovsky. 2013. Binding to F-actin guides cadherin cluster assembly, stability, and movement. *J. Cell Biol.* 201:131–143. http://dx.doi.org/10.1083/jcb.201211054

Hookway, C., L. Ding, M.W. Davidson, J.Z. Rappoport, G. Danuser, and V.I. Gelfand. 2015. Microtubule-dependent transport and dynamics of vimentin intermediate filaments. *Mol. Biol. Cell*. http://dx.doi.org/10.1091/mbc.E14-09-1398

Huen, A.C., J.K. Park, L.M. Godsel, X. Chen, L.J. Bannon, E.V. Amargo, T.Y. Hudson, A.K. Mongiu, I.M. Leigh, D.P. Kelsell, et al. 2002. Intermediate filament–membrane attachments function synergistically with actin-dependent contacts to regulate intercellular adhesive strength. *J. Cell Biol.* 159:1005–1017. http://dx.doi.org/10.1083/jcb.200206098

Kametani, Y., and M. Takeichi. 2007. Basal-to-apical cadherin flow at cell junctions. *Nat. Cell Biol.* 9:92–98. http://dx.doi.org/10.1038/ncb1520

Kljuic, A., H. Bazzi, J.P. Sundberg, A. Martinez-Mir, R. O'Shaughnessy, M.G. Mahoney, M. Levy, X. Montagutelli, W. Ahmad, V.M. Aita, et al. 2003. Desmoglein 4 in hair follicle differentiation and epidermal adhesion: evidence from inherited hypotrichosis and acquired pemphigus vulgaris. *Cell*. 113:249–260. http://dx.doi.org/10.1016/S0092-8674(03)00273-3

Koch, P.J., M.G. Mahoney, G. Cotsarelis, K. Rothenberger, R.M. Lavker, and J.R. Stanley. 1998. Desmoglein 3 anchors telogen hair in the follicle. *J. Cell Sci.* 111:2529–2537.

Lechler, T., and E. Fuchs. 2007. Desmoplakin: an unexpected regulator of microtubule organization in the epidermis. *J. Cell Biol.* 176:147–154. http://dx.doi.org/10.1083/jcb.200609109

le Duc, Q., Q. Shi, I. Blonk, A. Sonnenberg, N. Wang, D. Leckband, and J. de Rooij. 2010. Vinculin potentiates E-cadherin mechanosensing and is recruited to actin-anchored sites within adherens junctions in a myosin II–dependent manner. *J. Cell Biol.* 189:1107–1115. http://dx.doi.org/10.1083/jcb.201001149

Lee, C.H., M.S. Kim, B.M. Chung, D.J. Leahy, and P.A. Coulombe. 2012. Structural basis for heteromeric assembly and perinuclear organization of keratin filaments. *Nat. Struct. Mol. Biol.* 19:707–715. http://dx.doi.org/10.1038/nsmb.2330

Lei, K., X. Zhang, X. Ding, X. Guo, M. Chen, B. Zhu, T. Xu, Y. Zhuang, R. Xu, and M. Han. 2009. SUN1 and SUN2 play critical but partially redundant roles in anchoring nuclei in skeletal muscle cells in mice. *Proc. Natl. Acad. Sci. USA*. 106:10207–10212. http://dx.doi.org/10.1073/pnas.0812037106

Lombardi, M.L., and J. Lammerding. 2011. Keeping the LINC: the importance of nucleocytoskeletal coupling in intracellular force transmission and cellular function. *Biochem. Soc. Trans.* 39:1729–1734. http://dx.doi.org/10.1042/BST20110686

Lombardi, M.L., D.E. Jaalouk, C.M. Shanahan, B. Burke, K.J. Roux, and J. Lammerding. 2011. The interaction between nesprins and sun proteins at the nuclear envelope is critical for force transmission between the nucleus and cytoskeleton. *J. Biol. Chem.* 286:26743–26753. http://dx.doi.org/10.1074/jbc.M111.233700

Lüke, Y., H. Zaim, I. Karakesisoglou, V.M. Jaeger, L. Sellin, W. Lu, M. Schneider, S. Neumann, A. Beijer, M. Munck, et al. 2008. Nesprin-2 Giant (NUANCE) maintains nuclear envelope architecture and composition in skin. *J. Cell Sci.* 121:1887–1898. http://dx.doi.org/10.1242/jcs.019075

Luxton, G.W., E.R. Gomes, E.S. Folker, E. Vintinner, and G.G. Gundersen. 2010. Linear arrays of nuclear envelope proteins harness retrograde actin flow for nuclear movement. *Science*. 329:956–959. http://dx.doi.org/10.1126/science.1189072

Madison, K.C. 2003. Barrier function of the skin: "la raison d'être" of the epidermis. *J. Invest. Dermatol.* 121:231–241. http://dx.doi.org/10.1046/j.1523-1747.2003.12359.x

Malone, C.J., L. Misner, N. Le Bot, M.C. Tsai, J.M. Campbell, J. Ahringer, and J.G. White. 2003. The *C. elegans* hook protein, ZYG-12, mediates the essential attachment between the centrosome and nucleus. *Cell*. 115:825–836. http://dx.doi.org/10.1016/S0092-8674(03)00985-1

Martini, F.J., and M. Valdeolmillos. 2010. Actomyosin contraction at the cell rear drives nuclear translocation in migrating cortical interneurons. *J. Neurosci.* 30:8660–8670. http://dx.doi.org/10.1523/JNEUROSCI.1962-10.2010

Maruthamuthu, V., B. Sabass, U.S. Schwarz, and M.L. Gardel. 2011. Cell-ECM traction force modulates endogenous tension at cell-cell contacts. *Proc. Natl. Acad. Sci. USA*. 108:4708–4713. http://dx.doi.org/10.1073/pnas.1011123108

Mertz, A.F., S. Banerjee, Y. Che, G.K. German, Y. Xu, C. Hyland, M.C. Marchetti, V. Horsley, and E.R. Dufresne. 2012. Scaling of traction forces with the size of cohesive cell colonies. *Phys. Rev. Lett.* 108:198101. http://dx.doi.org/10.1103/PhysRevLett.108.198101

Mertz, A.F., Y. Che, S. Banerjee, J.M. Goldstein, K.A. Rosowski, S.F. Revilla, C.M. Niessen, M.C. Marchetti, E.R. Dufresne, and V. Horsley. 2013. Cadherin-based intercellular adhesions organize epithelial cell-matrix traction forces. *Proc. Natl. Acad. Sci. USA*. 110:842–847. http://dx.doi.org/10.1073/pnas.1217279110

Mirmirani, P., H. Uno, and V.H. Price. 2011. Abnormal inner root sheath of the hair follicle in the loose anagen hair syndrome: an ultrastructural study. *J. Am. Acad. Dermatol.* 64:129–134. http://dx.doi.org/10.1016/j.jaad.2010.01.026

Morioka, K. 2005. Inner root sheath. *In* Hair Follicle: Differentiation Under the Electron Microscope. Springer-Verlag, Tokyo, Japan. 63–88.

Nekrasova, O., and K.J. Green. 2013. Desmosome assembly and dynamics. *Trends Cell Biol.* 23:537–546. http://dx.doi.org/10.1016/j.tcb.2013.06.004

Nekrasova, O.E., E.V. Amargo, W.O. Smith, J. Chen, G.E. Kreitzer, and K.J. Green. 2011. Desmosomal cadherins utilize distinct kinesins for assembly into desmosomes. *J. Cell Biol.* 195:1185–1203. http://dx.doi.org/10.1083/jcb.201106057

Niessen, C.M., D. Leckband, and A.S. Yap. 2011. Tissue organization by cadherin adhesion molecules: dynamic molecular and cellular mechanisms of morphogenetic regulation. *Physiol. Rev.* 91:691–731. http://dx.doi.org/10.1152/physrev.00004.2010

Norden, C., S. Young, B.A. Link, and W.A. Harris. 2009. Actomyosin is the main driver of interkinetic nuclear migration in the retina. *Cell*. 138:1195–1208. http://dx.doi.org/10.1016/j.cell.2009.06.032

Oakes, P.W., Y. Beckham, J. Stricker, and M.L. Gardel. 2012. Tension is required but not sufficient for focal adhesion maturation without a stress fiber template. *J. Cell Biol.* 196:363–374. http://dx.doi.org/10.1083/jcb.201107042

Pasdar, M., K.A. Krzeminski, and W.J. Nelson. 1991. Regulation of desmosome assembly in MDCK epithelial cells: Coordination of membrane core and cytoplasmic plaque domain assembly at the plasma membrane. *J. Cell Biol.* 113:645–655. http://dx.doi.org/10.1083/jcb.113.3.645

Pelham, R.J., Jr., and Y. Wang. 1997. Cell locomotion and focal adhesions are regulated by substrate flexibility. *Proc. Natl. Acad. Sci. USA*. 94:13661–13665. http://dx.doi.org/10.1073/pnas.94.25.13661

Postel, R., M. Ketema, I. Kuikman, J.M. de Pereda, and A. Sonnenberg. 2011. Nesprin-3 augments peripheral nuclear localization of intermediate filaments in zebrafish. *J. Cell Sci.* 124:755–764. http://dx.doi.org/10.1242/jcs.081174

Rashmi, R.N., B. Eckes, G. Glöckner, M. Groth, S. Neumann, J. Gloy, L. Sellin, G. Walz, M. Schneider, I. Karakesisoglou, et al. 2012. The nuclear envelope protein Nesprin-2 has roles in cell proliferation and differentiation during wound healing. *Nucleus*. 3:172–186. http://dx.doi.org/10.4161/nucl.19090

Ray, S., H.P. Foote, and T. Lechler. 2013. β-Catenin protects the epidermis from mechanical stresses. *J. Cell Biol.* 202:45–52. http://dx.doi.org/10.1083/jcb.201212140

Razafsky, D., N. Blecher, A. Markov, P.J. Stewart-Hutchinson, and D. Hodzic. 2012. LINC complexes mediate the positioning of cone photoreceptor nuclei in mouse retina. *PLoS ONE*. 7:e47180. http://dx.doi.org/10.1371/journal.pone.0047180

Riveline, D., E. Zamir, N.Q. Balaban, U.S. Schwarz, T. Ishizaki, S. Narumiya, Z. Kam, B. Geiger, and A.D. Bershadsky. 2001. Focal contacts as mechanosensors: externally applied local mechanical force induces growth of focal contacts by an mDia1-dependent and ROCK-independent mechanism. *J. Cell Biol.* 153:1175–1186. http://dx.doi.org/10.1083/jcb.153.6.1175

Siegrist, S.E., and C.Q. Doe. 2007. Microtubule-induced cortical cell polarity. *Genes Dev.* 21:483–496. http://dx.doi.org/10.1101/gad.1511207

Simon, D.N., and K.L. Wilson. 2011. The nucleoskeleton as a genome-associated dynamic 'network of networks'. *Nat. Rev. Mol. Cell Biol.* 12:695–708. http://dx.doi.org/10.1038/nrm3207

Simpson, C.L., D.M. Patel, and K.J. Green. 2011. Deconstructing the skin: cytoarchitectural determinants of epidermal morphogenesis. *Nat. Rev. Mol. Cell Biol.* 12:565–580. http://dx.doi.org/10.1038/nrm3175

Sosa, B.A., A. Rothballer, U. Kutay, and T.U. Schwartz. 2012. LINC complexes form by binding of three KASH peptides to domain interfaces of trimeric SUN proteins. *Cell*. 149:1035–1047. http://dx.doi.org/10.1016/j.cell.2012.03.046

Stenn, K.S., and R. Paus. 2001. Controls of hair follicle cycling. *Physiol. Rev.* 81:449–494.

Strzyz, P.J., H.O. Lee, J. Sidhaye, I.P. Weber, L.C. Leung, and C. Norden. 2015. Interkinetic nuclear migration is centrosome independent and ensures apical cell division to maintain tissue integrity. *Dev. Cell*. 32:203–219. http://dx.doi.org/10.1016/j.devcel.2014.12.001

Sumigray, K.D., and T. Lechler. 2011. Control of cortical microtubule organization and desmosome stability by centrosomal proteins. *BioArchitecture*. 1:221–224. http://dx.doi.org/10.4161/bioa.18403

Sumigray, K.D., H. Chen, and T. Lechler. 2011. Lis1 is essential for cortical microtubule organization and desmosome stability in the epidermis. *J. Cell Biol.* 194:631–642. http://dx.doi.org/10.1083/jcb.201104009

Sumigray, K.D., H.P. Foote, and T. Lechler. 2012. Noncentrosomal microtubules and type II myosins potentiate epidermal cell adhesion and barrier formation. *J. Cell Biol.* 199:513–525. http://dx.doi.org/10.1083/jcb.201206143

Trepat, X., M.R. Wasserman, T.E. Angelini, E. Millet, D.A. Weitz, J.P. Butler, and J.J. Fredberg. 2009. Physical forces during collective cell migration. *Nat. Phys.* 5:426–430. http://dx.doi.org/10.1038/nphys1269

Tunggal, J.A., I. Helfrich, A. Schmitz, H. Schwarz, D. Günzel, M. Fromm, R. Kemler, T. Krieg, and C.M. Niessen. 2005. E-cadherin is essential for *in vivo* epidermal barrier function by regulating tight junctions. *EMBO J.* 24:1146–1156. http://dx.doi.org/10.1038/sj.emboj.7600605

Vaezi, A., C. Bauer, V. Vasioukhin, and E. Fuchs. 2002. Actin cable dynamics and Rho/Rock orchestrate a polarized cytoskeletal architecture in the early steps of assembling a stratified epithelium. *Dev. Cell*. 3:367–381. http://dx.doi.org/10.1016/S1534-5807(02)00259-9

Wang, N., J.D. Tytell, and D.E. Ingber. 2009. Mechanotransduction at a distance: mechanically coupling the extracellular matrix with the nucleus. *Nat. Rev. Mol. Cell Biol.* 10:75–82. http://dx.doi.org/10.1038/nrm2594

Wang, Y.C., Z. Khan, M. Kaschube, and E.F. Wieschaus. 2012. Differential positioning of adherens junctions is associated with initiation of epithelial folding. *Nature*. 484:390–393. http://dx.doi.org/10.1038/nature10938

Wittmann, T., and C.M. Waterman-Storer. 2005. Spatial regulation of CLASP affinity for microtubules by Rac1 and GSK3β in migrating epithelial cells. *J. Cell Biol.* 169:929–939. http://dx.doi.org/10.1083/jcb.200412114

Wu, S.K., G.A. Gomez, M. Michael, S. Verma, H.L. Cox, J.G. Lefevre, R.G. Parton, N.A. Hamilton, Z. Neufeld, and A.S. Yap. 2014. Cortical F-actin stabilization generates apical-lateral patterns of junctional contractility that integrate cells into epithelia. *Nat. Cell Biol.* 16:167–178. http://dx.doi.org/10.1038/ncb2900

Wu, X., A. Kodama, and E. Fuchs. 2008. ACF7 regulates cytoskeletal-focal adhesion dynamics and migration and has ATPase activity. *Cell*. 135:137–148. http://dx.doi.org/10.1016/j.cell.2008.07.045

Yonemura, S., Y. Wada, T. Watanabe, A. Nagafuchi, and M. Shibata. 2010. α-Catenin as a tension transducer that induces adherens junction development. *Nat. Cell Biol.* 12:533–542. http://dx.doi.org/10.1038/ncb2055

Yu, J., K. Lei, M. Zhou, C.M. Craft, G. Xu, T. Xu, Y. Zhuang, R. Xu, and M. Han. 2011. KASH protein Syne-2/Nesprin-2 and SUN proteins SUN1/2 mediate nuclear migration during mammalian retinal development. *Hum. Mol. Genet.* 20:1061–1073. http://dx.doi.org/10.1093/hmg/ddq549

Zhang, X., R. Xu, B. Zhu, X. Yang, X. Ding, S. Duan, T. Xu, Y. Zhuang, and M. Han. 2007. Syne-1 and Syne-2 play crucial roles in myonuclear anchorage and motor neuron innervation. *Development*. 134:901–908. http://dx.doi.org/10.1242/dev.02783

Zhao, T., O.S. Graham, A. Raposo, and D. St Johnston. 2012. Growing microtubules push the oocyte nucleus to polarize the *Drosophila* dorsal-ventral axis. *Science*. 336:999–1003. http://dx.doi.org/10.1126/science.1219147